International Journal of Biological Macromolecules 329 (2025) 147827

Contents lists available at ScienceDirect

International Journal of Biological Macromolecules

journal homepage: www.elsevier.com/locate/ijbiomac

# Dual cations cross-linked alginate-kaolin hydrogel beads for chlortetracycline hydrochloride loading: Preparation, characterization, loading mechanism, *in-vitro* release studies, and antibacterial activity assessment

Wei Liu [a,*,1], Fizir Meriem [b,c,**,1], Touil Sami [b], Richa Amina [b], Benaissa Fatiha [b], Bensettou Chaimaa [b], Douba Houda [c,d], Tingzi Cao [a], Aouameur Djamila [b], Xiaowei Tu [a], Jing Ding [a], Dramou Pierre [e,*]

[a] Zhejiang Pharmaceutical University, Ningbo, 315500, Zhejiang, China
[b] Laboratory of Precision Agriculture, Environment and Sustainable Development, Khemis Miliana University, Algeria
[c] Laboratoire de Valorisation des Substances Naturelles, University of Khemis Miliana, Algeria.
[d] Laboratory Physical Chemistry of Materials Interfaces Applied to the Environment, University of Saad Dahlab Blida 1, Algeria
[e] Department of Analytical Chemistry, School of Sciences, China Pharmaceutical University, Nanjing, 210009, Jiangsu, China

ARTICLE INFO

*Keywords:*
Kaolin
Alginate
Chlortetracycline hydrochloride
Adsorption
Sustained release

ABSTRACT

This study aims to evaluate the performance of dual cation cross-linked alginate-kaolin hydrogel beads (Fe/Ca-Alg@K) as drug delivery system, and comprehensively investigate the mechanisms of CTC drug loading and sustained release profile, while also assessing their antibacterial efficacy for potential therapeutic applications. The synthesized hydrogel beads were characterized by SEM, EDS, FTIR, BET, TGA, and XPS confirming their porous architecture, stable chemical structure, and enhanced thermal stability. Incorporating kaolin significantly improved drug encapsulation efficiency, reaching up to 89.47 ± 1.6 %, and a loading capacity of 317.03 ± 1.4 mg/g, while dual cross-linking with $Ca^{2+}$ and $Fe^{3+}$ ions further strengthened the matrix network and improved drug adsorption capacity and encapsulation efficiency. The adsorption mechanism of CTC onto Fe/Ca-Alg@K hydrogel beads revealed multiple interactions involving both the functional groups of beads and the elemental components (Si and Al) of K. *In vitro* drug release studies revealed that Fe/Ca-Alg@K could sustain the release of CTC, and the release profile was best described by quasi-Fickian diffusion at pH 1.2, while controlled by diffusion combined with polymer swelling and erosion in pH 7.4. Antibacterial assays confirmed the bioactivity of released CTC. The developed composite system shows promise for controlled drug delivery and localized antibacterial therapies.

## 1. Introduction

The increasing prevalence of antibiotic resistance, coupled with the limitations of conventional drug delivery systems, has heightened the need for the development of novel and more effective drug carriers. Traditional drug delivery strategies frequently fail to address issues of rapid drug release, poor bioavailability, and inadequate localization of therapeutic agents at the target site [1,2]. To overcome these challenges, there is growing interest in the design of advanced drug delivery systems capable of controlled, sustained, and targeted release [3].

Natural polymers such as proteins and polysaccharides are widely used in biomedical applications owing to their biocompatibility and *in vivo* biodegradability [1,2]. Sodium alginate (SA), a natural polysaccharide derived from brown algae (*e.g.*, kelp, sargassum), has a backbone of alternately arranged guluronic (G) and mannuronic (M) acid units [4]. Alginate-based hydrogels can be synthesized through diverse cross-linking strategies, offering advantages including low cost, high water-absorption capacity, biocompatibility, excellent drug-

* Corresponding authors.
** Correspondence to: F. Meriem, Laboratory of Precision Agriculture, Environment and Sustainable Development, Khemis Miliana University, Algeria.
*E-mail addresses:* liuw@zjpc.net.cn (W. Liu), meriem.fizir@univ-dbkm.dz (F. Meriem), 1620164347@cpu.edu.cn (D. Pierre).
[1] The authors contributed equally to this work.

https://doi.org/10.1016/j.ijbiomac.2025.147827
Received 18 May 2025; Received in revised form 11 September 2025; Accepted 19 September 2025
Available online 22 September 2025

loading capabilities, and tunable biodegradation [5,6]. Notably, structural congruence with biological extracellular matrices (ECM) enables their application across wound healing, therapeutic delivery systems, and cell transplantation [4,7]. Drug molecules, spanning from small chemical entities to large protein therapeutics, can be controllably released from alginate-based hydrogels, with their release kinetics dictated by the type of cross-linker and cross-linking methodology [4,7]. For instance, sodium ions in alginate monomers can undergo ion exchange with polyvalent cations (*e.g.*, $Ca^{2+}$, $Fe^{3+}$, $Ba^{2+}$), inducing electrostatic interactions between adjacent polymer chains to form a three-dimensional "egg-box" network structure [4,8]. Specifically, calcium beads crosslinked with SA effectively shield acid-sensitive drugs from gastric acid, preserving them until gradual release in the intestine [9]. Martínez-Gómez et al.'s study further highlights the potential of sodium alginate/polyvinyl alcohol hydrogels for controlled drug release in the intestinal environment [10]. However, one of the major limitations of single-ion cross-linked alginate hydrogels is their low mechanical strength [4] and relatively poor control over drug diffusion, which can lead to unpredictable release profiles.

To overcome these limitations, various strategies have been implemented to regulate drug release profiles and swelling behavior. Current approaches include optimizing beads fabrication processes, adjusting material ratios, constructing three-dimensional network structures, and incorporating nanofillers to enhance the release performance of alginate-based polymer matrices [11,12]. Some studies have reported that the incorporation of multi-walled carbon nanotubes (MWCNTs) or graphene oxide (GO) composites can effectively reduce the initial burst drug release [13,14]. Nevertheless, concerns regarding potential cytotoxicity and high production costs significantly diminish the attractiveness of these materials for large-scale biomedical applications. This critical limitation highlights the urgent need to develop novel low-cost materials as alternative solutions for advanced drug delivery systems.

Clay minerals, which are widely sourced, inexpensive, and biocompatible, are frequently used as pharmaceutical excipients in various drug formulations [15]. Consequently, researchers have attempted to utilize mineral clays, such as bentonite and montmorillonite, as alternatives to materials like MWCNTs and GO, in combination with SA, to prepare drug-loaded microspheres, achieving promising results [4,16]. Among the numerous clay minerals, kaolin (K), with the chemical composition of $Al_2Si_2O_5(OH)_4$, exhibits biocompatibility and a lower cost compared to montmorillonite [17]. Its high porosity, large specific surface area, and abundant hydroxyl groups on its surface enable it to interact with various organic and inorganic molecules, providing excellent drug-loading capabilities. These properties endow kaolin with exceptional adsorption and drug-loading capacities, making it a frequently utilized material for controlled-release drug carriers [17,18].

Based on our earlier research findings, it has been confirmed that beads prepared using $Fe^{3+}$ cross-linked alginate-based K exhibit excellent adsorption properties [19]. Additional studies have compared the sustained-release effects of curcumin in beads prepared by incorporating $Ca^{2+}$ along with ions such as $Mg^{2+}$, $Ba^{2+}$, $Al^{3+}$, among others, as dual-ion cross-linking agents into a SA/montmorillonite matrix. These studies revealed that cross-linking with different ions can significantly influence the sustained-release efficiency of drugs. In particular, compared to single $Ca^{2+}$ cross-linking, CaAl dual cross-linked carriers exhibit lower water absorption swelling rates and possess a more rigid cross-linked structure, thereby achieving superior sustained-release effects [4]. Thus, dual ion cross-linking also is a promising strategy [20]. By incorporating two different cations as cross-linkers, it is possible to enhance the structural integrity of the hydrogel network, improve its mechanical properties, and modulate the release rate of encapsulated drugs [4]. The application of SA/K beads cross-linked with $Ca^{2+}$, $Fe^{3+}$, or other metal ions in drug delivery systems, and the mechanisms of adsorption and release of drugs by these beads still required further in-depth exploration.

Chlortetracycline hydrochloride (CTC) is a broad-spectrum antibiotic commonly used in veterinary and human medicine [21]. Despite its wide usage, CTC is prone to rapid degradation and exhibits limited bioavailability when administered through conventional formulations [22]. Encapsulating of CTC in a stable delivery system that can provide controlled and sustained release would not only improve its therapeutic efficacy but also reduce side effects associated with high peak concentrations [23]. In this work, we present the synthesis and characterization of dual cation cross-linked alginate-kaolin hydrogel beads for the controlled delivery of CTC. The study aims to optimize the encapsulation efficiency by adsorption equilibrium, release profile, and antibacterial activity of the composite system, providing a promising approach for the development of controlled drug delivery systems with enhanced performance.

## 2. Materials and methods

### 2.1. Materials

Ferric chloride ($FeCl_3$) and calcium chloride ($CaCl_2$) were obtained from Shanghai Aladdin Biochemical Technology Co., Ltd. Chlortetracycline hydrochloride (CTC, chemical formula $C_{22}H_{23}ClN_2O_8$, with a molecular weight of 478.88 g/mol) was purchased from Merck, and Kaolin was provided by Tianjin Fuchen Fine Chemical Co., Ltd. in China. Sodium alginate was purchased from Dengfeng Chemical Reagent Factory in Tianjin, China. Other reagents are from China National Pharmaceutical Group Chemical Reagent Co., Ltd. All reagents were of analytical grade.

### 2.2. Preparation of dual cross-linked alginate-kaolin beads

The alginate beads based K were synthesized using the extrusion method [24]. Briefly, 2 g of SA was firstly dissolved in 100 mL of distilled water and stirred to form a gel solution. Next, 2 g of K was mixed evenly with the stirred gel solution for 2 h at room temperature. Subsequently, the suspension settled gradually in a uniform alginate-kaolin solution. This mixture was then added drop wise into a container with a 2 % ($Fe^{3+}$/$Ca^{2+}$) solution using a dropper. The $Ca^{2+}$ and $Fe^{3+}$ caused the alginate-kaolin mixture to cross-link immediately upon contact with the solution, forming beads. These beads were allowed to harden for 24 h. After solidification, the beads were rinsed thoroughly with distilled water to remove excess $CaCl_2$ and $FeCl_3$, resulting in raw beads with an average size of 3.8 mm, which were kept in distilled water for further use. Some of raw beads were transformed into oven for 60 °C/12 h to obtain dried beads. The designation scheme for experimental samples and the detailed compositional parameters of the prepared formulations is documented in Table 1. The method for preparing dual cross-linked alginate-kaolin beads is shown in Fig. 1.

### 2.3. CTC loading to alginate beads based on K series

The adsorption equilibrium method was selected to load CTC onto various beads formulations. This approach is widely favored in drug delivery applications due to its simplicity, ability to preserve drug structure and bioactivity (unlike covalent bonding, which may alter drug properties), and its versatility in designing stimulus-responsive drug carriers [25]. Various parametric studies were performed to optimize of loading (adsorption) capacity including physical state of beads (wet and dry), SA concentration of beads (2 %–4 %), different amount of beads Fe/Ca-Alg@K4 (100, 200, 300, 400, 500, 750, and 1000 mg, respectively), different shaking speeds (100, 150, 200, and 250 rpm), the pH of a CTC solution (pH 2–12), contact time (10 min to 4 h), and initial CTC concentration (10–200 mg/L). Adsorption was achieved by mixing a CTC solution with a specified quantity of beads in a 125 mL flask. The contents were shaken for 4 h. The supernatant was then centrifuged at 3000 rpm for 5 min to determine CTC concentration by a *UV* spectrophotometer. The loading capacity (mg/g), and the

**Table 1**
Designation and detailed compositional parameters of the prepared experimental samples.

| Designation | Description | Concentration of SA (%) | Mass of K (g) | Mass of cross-linkers (g) |
|---|---|---|---|---|
| Fe/Ca-Alg | Fe/Ca cross-linked SA hydrogel beads | 2 | 0 | 5 g $FeCl_3$/ 5 g $CaCl_2$ |
| Fe-Alg@K | Fe cross-linked SA based K hydrogel beads | 2 | 2 | 10 g $FeCl_3$ |
| Ca-Alg@K | Ca cross-linked SA based K hydrogel beads | 2 | 2 | 10 g $CaCl_2$ |
| Fe/Ca-Alg@K | Dual Fe/Ca cross-linked SA based K hydrogel beads-2 | 2 | 2 | 5 g $FeCl_3$/ 5 g $CaCl_2$ |
| Fe/Ca-Alg@K3 | Dual Fe/Ca cross-linked SA based K hydrogel beads-3 | 3 | 2 | 5 g $FeCl_3$/ 5 g $CaCl_2$ |
| Fe/Ca-Alg@K4 | Dual Fe/Ca cross-linked SA based K hydrogel beads-4 | 4 | 2 | 5 g $FeCl_3$/ 5 g $CaCl_2$ |

encapsulation efficiency (EE) of the beads (adsorbents) were calculated using Eqs. (1), and (2), respectively [26].

$$Q = \frac{(C_0 - C_e) \times V}{m} \tag{1}$$

$$EE(\%) = \frac{\text{total drug quantity adsorbed (g)}}{\text{actual drug quantity (g)}} \times 100\% \tag{2}$$

where, $Q$ is the drug loading (adsorption) capacity of the beads (CTC mg/dry beads g), $V$ represents the volume of the reaction solution (mL), $m$ denotes the mass of the adsorbents (g), $C_0$ and $C_e$ stands for the initial and equilibrium concentration of CTC (mg/L) in the solution.

### 2.4. Swelling test of beads

The swelling behavior of beads after CTC adsorption with various formulations was evaluated by weight analysis in pH 7.4 and pH 1.2. The swelling degree is obtained by the following Eq. (4) [3]:

$$Swelling\ degree(\%) = \frac{W_s - W_d}{W_d} \times 100\% \tag{3}$$

where $W_s$ (g) and $W_d$ (g) was the weight of the beads after and before swelling, respectively.

### 2.5. Characterization

The morphology of the bead adsorbents before and after CTC adsorption was investigated using scanning electron microscopy (SEM) and energy dispersive spectroscopy mappings (EDS, colored). To enhance conductivity, the beads were coated with Platinum (Pt), then scanned and analyzed for elemental composition before and after their interaction with CTC using a Hitachi Regulus 8100 SEM equipped with EDS, at a voltage of 5.0 kV. The structural characteristics of the beads were analyzed using X-ray Diffraction (XRD) on a Bruker D8 ADVANCE system, equipped with Cu Kα radiation. The system parameters record data within a $2\theta$ range of 5°–80° at a scanning rate of 8°/min. The changes in functional groups in Fe/Ca-Alg@K4 (before CTC adsorption) and Fe/Ca-Alg@K4@CTC (after CTC adsorption) were studied using Fourier transform infrared spectroscopy (FT-IR8400 spectrometer, SHIMADZU, Japan). The X-ray photoelectron spectroscopy (XPS) was conducted using ESCALAB 250Xi, Thermo, USA. The surface textural properties of the adsorbents were observed by BET surface analyzer (ASAP2020, Micromeritics, USA) at $N_2$ atmosphere. Thermogravimetric analysis (TGA) used STA 449 F5 Jupiter®, NETZSCH, Germany. The dried sample was accurately weighed, and nitrogen ($N_2$) was utilized as the carrier gas for the test. The temperature range for the analysis was set from 30 °C to 800 °C, with a heating rate of 10 °C/min.

### 2.6. In vitro release study of CTC

The release of CTC from the hydrogel beads was evaluated in simulated gastric fluid (pH 1.2) and intestinal fluid (pH 7.4) at 37 ± 0.5 °C. Dried beads loaded with CTC drugs were placed in the release medium (100 mL) and incubated under shaking (100 rpm). At specific time intervals, 4 mL of aliquots were withdrawn, filtered, and analyzed spectrophotometrically at 365 nm. Fresh simulated solution (4 mL) was added to maintain sink conditions. Release profiles were plotted, and cumulative drug release (%) was calculated.

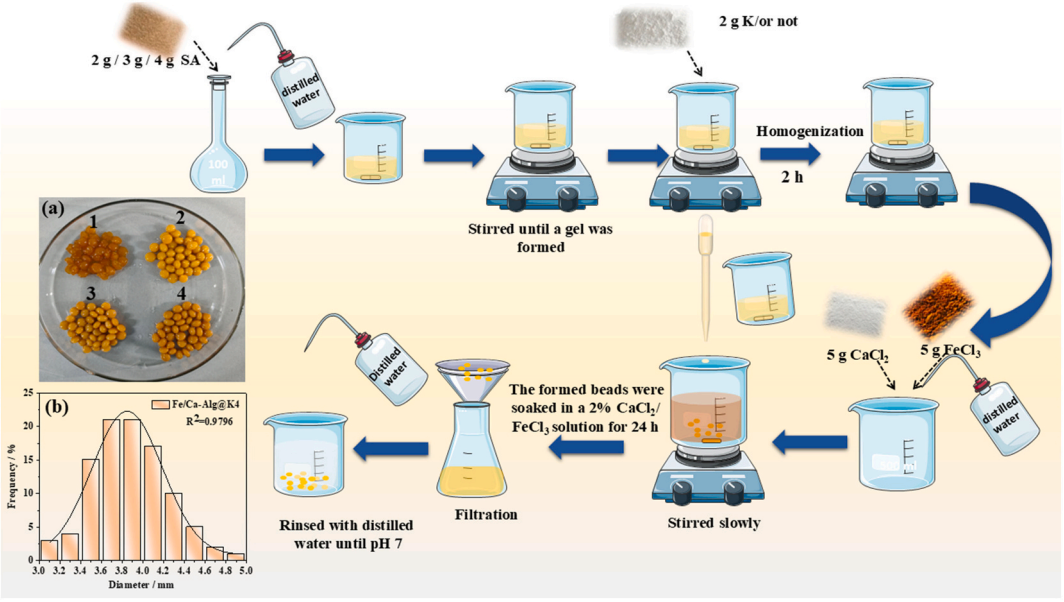


**Fig. 1.** Preparation method of dual cross-linked alginate-kaolin beads. Illustration (a) Synthesized beads (1: Fe/Ca-Alg, 2: Fe/Ca-Alg@K, 3: Fe/Ca-Alg@K3, 4: Fe/Ca-Alg@K4. (b) The particle size distribution diagram of the Fe/Ca-Alg@K4 wet bead.

$$\text{Cumulative drug release}(\%) = \frac{C_{release}}{C_{total}} \times 100\% \quad (4)$$

where $C_{release}$ and $C_{total}$ are the cumulative concentration of beads released drug in the solution at time t and the total drug loading concentration, respectively.

### 2.7. Release kinetics modeling

The *in vitro* release data were fitted to zero-order, first-order, Higuchi, and Korsmeyer-Peppas models to elucidate the drug release mechanisms [27,28]. The equations of these four models are as follows:

Zero-order model equation:

$$M_t = M_0 + K_0 t \quad (5)$$

First order model equation:

$$\log M_t = log M_0 - K_1 t/2.303 \quad (6)$$

Higuchi model equation:

$$M_t/M_\infty = K_H t^{1/2} \quad (7)$$

Korsmeyer–Peppas model equation:

$$\log(M_t/M_\infty) = \log(K_{kp}) + n\log(t) \quad (8)$$

where $M_t$ corresponds to the cumulative drug released at time $t$, while $M_\infty$ represents the maximum achievable drug loading, $K$ represents the release rate constant. Correlation coefficients ($R^2$) and release exponents ($n$) were used to interpret the predominant transport phenomena. Specifically, quasi-Fickian transport is characterized by $n < 0.5$, Fickian diffusion characterized by the drug diffusing and releasing out of the polymer matrix by $n = 0.5$, and non-Fickian or anomalous transport phenomena by $0.5 < n < 1.0$ [28].

### 2.8. Antibacterial activity

Based on the agar diffusion test, antibacterial experiments were conducted on K, and beads including Fe/Ca-Alg@K, Fe/Ca-Alg@K3, and Fe/Ca-Alg@K4, as well as their CTC-encapsulated beads, against *Escherichia coli* (*E. coli*, Gram-negative) (ATCC 25923) and *Staphylococcus aureus* (*S. aureus*, Gram-positive) (ATCC 25922). Specifically, bacterial spore suspensions (0.5 McFarland) were inoculated onto solid agar plates. Subsequently, the beads were aseptically inoculated onto the agar surface, and cultures were then incubated at 37 °C condition kept for 24 h. Bacterial growth inhibition zones were visually inspected and measured in millimeters. Following incubation, inhibition zones surrounding each sample were measured, and the antibacterial effect was recorded [29].

### 2.9. Statistical analysis

All experiments were independently replicated three times to ensure the reliability of the data. Data were expressed as mean ± standard deviation (SD). Statistical analysis was carried out using one-way ANOVA and Post-Hoc multiple comparisons were determined by Tukey's test (IBM SPSS Statistics V20.0, GraphPad PrismV9.0.0.121), with $p < 0.05$ considered statistically significant.

## 3. Results and discussion

### 3.1. CTC loading and encapsulation efficiency onto Fe/Ca-Alg@K beads

#### 3.1.1. The effect of the physical state and the type of crosslinking agent of beads

As shown in Fig. 2a, there were significant differences between beads cross-linked with different cations. Additionally, significant differences were observed between their dry and wet states ($p < 0.05$). The adsorption differences between the dry and wet states of the beads may be attributed to their porous structure. When the beads were dried, their porosity was insufficient to allow CTC to reach the active sites within the beads. Similar observations were also made by Rassis et al., who found that drying calcium alginate gels containing bentonite resulted in significant densification and smaller pore sizes [30]. In contrast, when the beads were in a wet state, the EE of CTC was higher, reaching a maximum of 89.32 % in Fe/Ca-Alg@K beads. This improvement could be primarily driven by extensive water retention within the wet beads, which increased their weight and facilitated the adsorption process.

Further investigation into the encapsulation of CTC by Alg@K crosslinked with various metal cations, particularly $Ca^{2+}$, $Fe^{3+}$, and a mixture of $Ca^{2+}$ and $Fe^{3+}$ (Fig. 2a), revealed that Alg@K beads crosslinked with a mixture of $Ca^{2+}$/$Fe^{3+}$ and Alg@K beads crosslinked with $Fe^{3+}$ exhibited higher CTC loading capacity compared to Alg@K beads crosslinked with $Ca^{2+}$ alone. This could be attributed to the dual crosslinking potential of $Fe^{3+}$ and $Ca^{2+}$, also clearly demonstrating the advantages of alginate hydrogels containing $Fe^{3+}$. The hydroxyl and carboxyl groups in CTC could serve as ligands and coordinate with $Fe^{3+}$ ions to form complexes. Furthermore, the higher charge of $Fe^{3+}$ allows for stronger electrostatic interactions with negatively charged CTC than $Ca^{2+}$, leading to the formation of more stable and robust complexes [20]. On the other hand, $Ca^{2+}$ crosslinked hydrogel beads exhibit superior swelling performance compared to $Fe^{3+}$ crosslinked ones [31]. During the adsorption process, the $Ca^{2+}$ crosslinked beads can swell more fully, resulting in a significant increase in their internal water content, and consequently enhancing the adsorption capacity for CTC.

Thus, based on this comparative study, it demonstrated that wet Fe/Ca-Alg@K beads could more effectively encapsulate CTCs. The presence of water within the beads improved the adsorption process, while the synergistic combination of $Fe^{3+}$ and $Ca^{2+}$ cross-linkers in the alginate beads significantly enhanced both swelling capacity and loading capacity compared to beads formed with either ion alone.

#### 3.1.2. The effect of SA concentration

The concentration of SA can affect the density of the gel mesh formed in beads and the encapsulation process of CTC within them [32]. However, in our study, increasing the SA concentration from 2 % to 4 % did not impact the EE or adsorption capacity (Fig. 2b). The EE of all studied formulations were similar, with values of 89.32 % ± 2.2 %, 88.69 % ± 1.8 %, and 89.47 % ± 1.6 % for Fe/Ca-Alg@K, Fe/Ca-Alg@K3, and Fe/Ca-Alg@K4, respectively, with no significant differences observed between groups ($p > 0.05$). The reason for this phenomenon may attribute to loading of CTC on the beads involves both chemical and physical interactions. Although Fe/Ca-Alg@K4 hydrogel beads, with a higher sodium alginate concentration (4 % SA), contains a higher total number of active sites capable of interacting with CTC, their denser network restricts diffusion. Conversely, the Fe/Ca-Alg@K hydrogel beads with lower SA concentration (2 %, 3 %) exhibit a looser gel network and larger pore size [32,33], allowing for greater CTC diffusion, thereby partially offsetting the advantage conferred by the higher concentration of active sites. These results suggested that within the studied concentration range, the amount of SA was not a limiting factor in adsorption process. Due to its higher EE and stable morphology, higher concentration of SA will form a denser cross-linked network more stable, reducing the rapid degradation after oral administration and improving the sustained release effect [32,34]. Therefore, Fe/Ca-Alg@K4 was selected for further study.

#### 3.1.3. The effect of beads dosage

The beads dosage determines the total number of active sites available for adsorption and it is a significant factor balancing efficiency and cost. The impact of bead dosage on the adsorption of 50 mg/L CTC for 4 h was investigated by varying the bead mass from 100 to 1000 mg. A minimum sample mass of 100 mg was established for adsorption

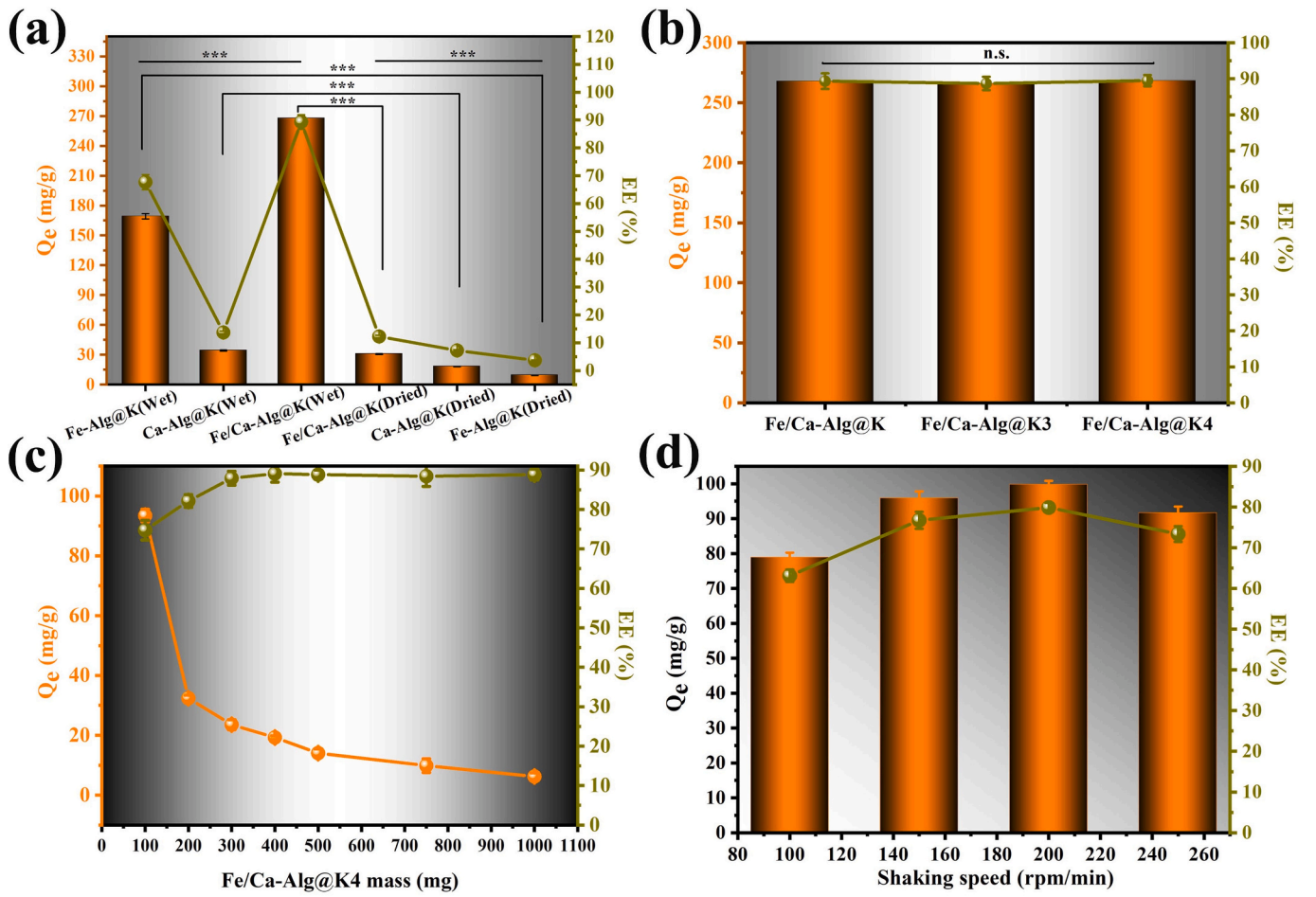


**Fig. 2.** (a) The influence of the physical state of beads and the type of crosslinking agent (*** in the figure indicate significant differences between groups, $p < 0.001$), (b) SA concentration in beads (n.s. in the figure indicate non-significant between groups, $p > 0.05$), (c) Fe/Ca-Alg@K4 beads mass, and (d) shaking speed on the adsorption capacity and EE of CTC.

experiments to facilitate practical handling and avoid the need for subsampling, which is error-prone with smaller, wet alginate beads. The encapsulation efficiency of CTC increased with beads mass (Fig. 2c), peaking at 89.08 % at a dosage of 400 mg, indicating that bead dosage provided more adsorption sites. Despite the increase in total binding sites, the adsorption capacity per unit mass of beads decreased due to inefficient utilization of active sites at higher dosages. This led to higher encapsulation efficiency and lower residual CTC concentration in the solution. Consequently, an optimal bead dosage of 100 mg was selected for achieving the maximum adsorption capacity performance (93.43 mg/g) and a satisfactory encapsulation efficiency (74.75 %) under 50 mg/L CTC concentration condition. Table 2 indicated that Fe/Ca-Alg@K4 has the higher encapsulation efficiency and adsorption capacity compared to K and Fe/Ca-Alg beads. This suggested that K significantly enhanced the loading capacity of CTC by providing more binding sites for the alginate network.

### 3.1.4. The effect of shaking speed

Shaking is a crucial factor in any mass transfer process because it enhances the contact between the adsorbent and adsorbate, thereby promoting adsorption. To investigate the effect of shaking speed on CTC adsorption, tests were conducted varying shaking rates (100–250 rpm) while maintaining other predetermined optimal parameters. The lower limit of 100 rpm was selected based on preliminary trials indicating low adsorption at 50 rpm. As illustrated in Fig. 2d, the optimal shaking speed was 200 rpm, which resulted in the maximum adsorption capacity and EE, 99.84 mg/g and 79.87 %, respectively. This speed proved to be sufficient to facilitate contact between Fe/Ca-Alg/K4 beads and CTC. At shaking speeds of 100 to 150 rpm, the adsorption of CTC onto Fe/Ca-Alg/K4 beads was relatively slow and gradually increased. The corresponding EE values were 63.12 % and 76.75 %, respectively. This phenomenon is attributed to solution turbulence thins boundary layers surrounding sorbent particles, accelerating CTC diffusion from bulk liquid to interfaces [35,36]. Conversely, a high shaking rate (250 rpm), significantly reduced adsorbate-adsorbent contact time, suppressing adsorption and resulting in a decrease in CTC adsorption capacity and EE to 91.71 mg/g and 73.37 %, respectively [35,36].

**Table 2**
The adsorption capacity and EE of CTC on K, Fe/Ca-Alg, and Fe/Ca-Alg@K4 beads.

| | K | Fe/Ca-Alg | Fe/Ca-Alg@K4 |
|---|---|---|---|
| Q (mg/g) | 43.75 | 78.125 | 93.43 |
| EE (%) | 35.00 | 46.875 | 74.75 |

### 3.1.5. The effect of solution pH

The influence of solution pH on adsorption behavior of CTC by Fe/Ca-Alg@K4 beads was investigated within the pH range from 2 to 11. As displayed in Fig. 3(a–b), the strongest adsorption of CTC and the highest EE on Fe/Ca-Alg@K4 were observed at pH values between 4 and 8, followed by a slight decrease with increasing pH. Optimal loading capacity and EE (99.84 mg/g and 79.87 %, respectively) were observed at pH 6. In fact, the predominant CTC species, classified according to

solution pH, are $CTCH^{3+}$, $CTCH^{2\pm}$, $CTCH^{-}$, and $CTC^{2-}$ when pH < 3.3, 3.3 < pH < 7.44, 7.44 < pH < 9.27, and pH > 9.27, respectively (Fig. 3c) [37,38]. The $pH_{pzc}$ value of Fe/Ca-Alg@K4 was measured to be approximately 4.1 (Fig. 3d), revealing that the hydrogel bead surface is positively charged when pH < $pH_{pzc}$, whereas a negative surface charge develops at pH > pHpzc. At pH < 4, the strong electrostatic repulsion between CTC species ($CTC^{+}$) and the positively charged surface of the beads (Fe/Ca-Alg@K4) hindered the adsorption of CTC, leading to poor adsorption performance. Conversely, when the pH was in the range of 4 to 8, CTC molecules was positive while Fe/Ca-Alg@K4 was changed to negative, which interact through electrostatic interactions ($CTCH^{2\pm}$-$X^{-}$) [37]. Thus, the enhanced interaction between Fe/Ca-Alg@K4 resulted in higher adsorption capacity for CTC. While the pH surpassed 8, a slight decrease in adsorption capacity occurred, due to electrostatic repulsion. Additionally, despite the potential positive-positive electrostatic repulsion at pH values below 4 and negative-negative electrostatic repulsion at pH values above 8, the adsorption capacity remained relatively high. Data showed that the adsorption capacity was 71.87–86.40 mg/g (pH 2–3) and 74.21–81.87 mg/g (pH 9–11). This indicated that the adsorption of CTC onto Fe/Ca-Alg@K4 beads is not primarily controlled by electrostatic interactions. Instead, other major interactions, such as negative charge-assisted hydrogen bonds, chelation or complexation, ligand exchange, and n-π interactions, may be responsible for this behavior. These results are consistent with previous studies [39,40].

Additionally, it can be observed that when the pH is below 4, a high concentration of $H^{+}$ ions compete with CTC for adsorption sites on Fe/Ca-Alg@K4 beads, leading to suppressed CTC adsorption. This observation is supported by the rise in final pH. In strongly alkaline conditions, the final decrease in pH can be attributed to the higher affinity of $OH^{-}$ ions for adsorption compared to CTC on the surface of the beads. This interaction reduces the concentration of $OH^{-}$ ions in the solution, further impacting the overall pH.

### 3.1.6. The effect of contact time

Analysis of the reaction time data revealed the equilibrium adsorption capacity and adsorption kinetics parameters for CTC loading onto the beads [41]. Fig. 4a illustrated the adsorption behavior and EE of CTC onto Fe/Ca-Alg@K4 beads. Three different regions were observed in the adsorption process curve, an initial rapid adsorption, followed by gradually increased and stabilized at 49.38 mg/g for 25 mg/L and 109.53 mg/g for 50 mg/L in a similar manner after about 180 min. On the other hand, increasing the initial concentration of CTC resulted in a decrease in EE (%) (Fig. 4b), potentially attributed to insufficient active sites on the beads surface to adsorb higher concentrations of CTC.

### 3.1.7. Dynamics research

To study the CTC adsorption mechanism, adsorption kinetics on the beads were analyzed using pseudo-first-order (PFO) and pseudo-second-order (PSO) models. The PFO describes a single-step adsorption process, while the PSO assumes a multi-step, more complex mechanism, with their nonlinear equations provided in Table S1. There are two main criteria for determining an appropriate kinetic model that corresponds to experimental data. The determination coefficient $R^2$ of an appropriate dynamic model must be greater than $R^2$ of other application models, and there is an analogy between $Q_{e(exp)}$ and $Q_{e(cal)}$ of the appropriate model. As displayed in Fig. 5a, at the initial stage of adsorption, CTC with two

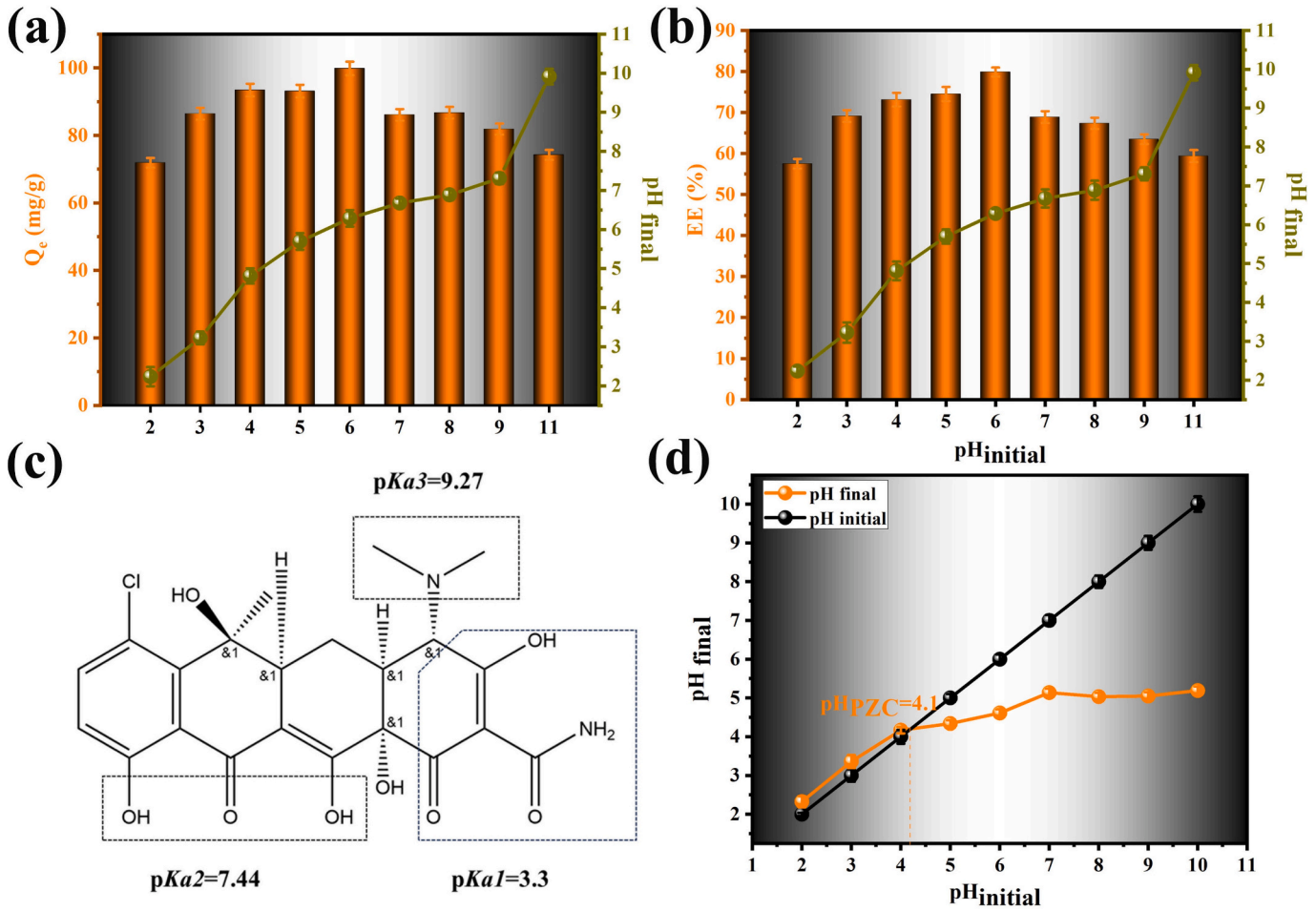


**Fig. 3.** The impact of solution pH evolution during adsorption and its effect on CTC adsorption capacity (a) and EE (b) for Fe/Ca-Alg@K4, the chemical structure of CTC, its three acid dissociation constants (pKa) (c), and the$pH_{PZC}$ of Fe/Ca-Alg@K4 (d).

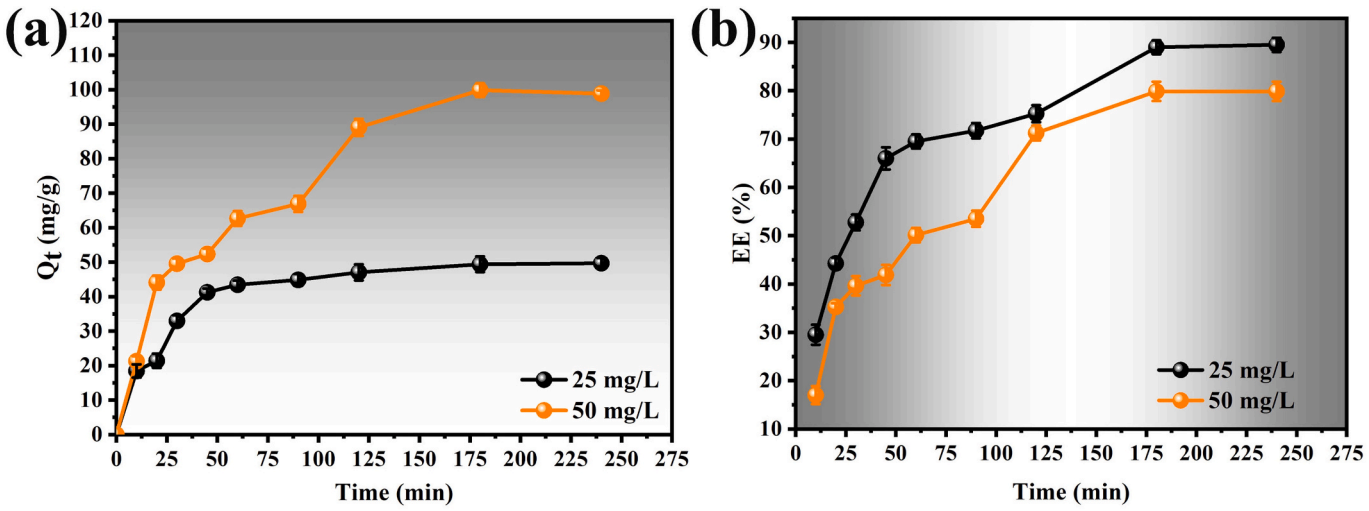


**Fig. 4.** The effect of time on CTC adsorption (a) and EE (b) on Fe/Ca-Alg@K4 at two different initial CTC concentrations (25 and 50 mg/L).

different concentrations was rapidly adsorbed and then the adsorption rate declined as the active sites became progressively occupied by CTC molecules, ultimately achieving equilibrium states with $Q_e$ of 49.68 mg/g and 99.84 mg/g, respectively. Both models had high $R^2$ values (>0.94) (Table 3). This indicated that the loading process was controlled by chemical and physical adsorption mechanisms. Furthermore, the better fit of pseudo-first-order $Q_e$ values to experimental results demonstrates that physisorption predominates [42].

To further clarify the adsorption mechanism and rate-controlling steps, the Weber Morris intraparticle diffusion (IPD) model was analyzed [43]. A plot of $Q_t$ *vs.* $t$ passing through the origin indicates intraparticle diffusion as the dominant factor, while deviation from the origin suggests it is not the sole rate-limiting step [44]. Therefore, CTC adsorption on the beads involved multiple processes, such as, surface adsorption, interparticle diffusion, and intraparticle diffusion (Fig. 5b) [40].

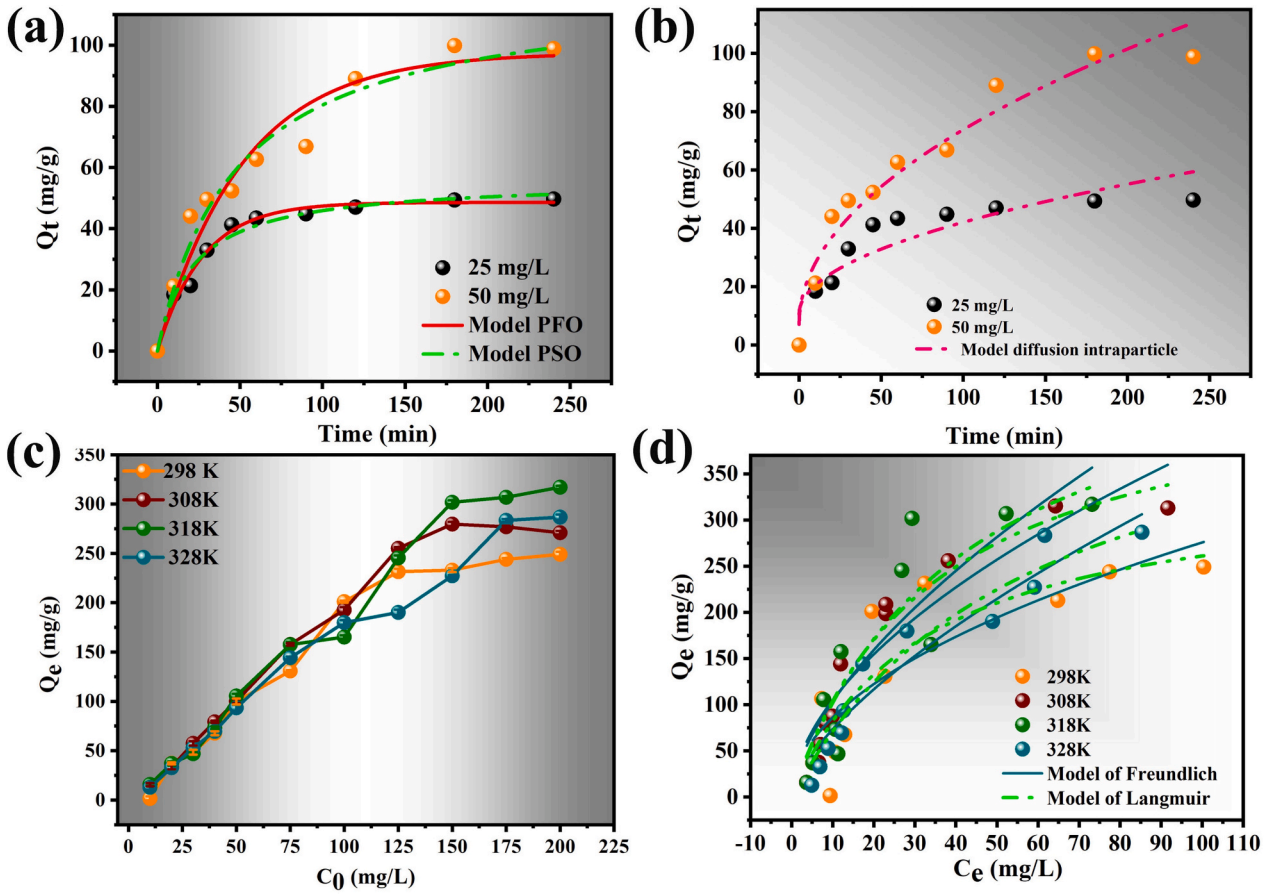


**Fig. 5.** (a) PFO and PSO kinetic models (b) IPD for CTC adsorption on Fe/Ca-Alg@K4 beads with initial CTC concentrations of 25 and 50 mg/L. (c) The effect of initial concentration on the adsorption capacity of CTC for Fe/Ca-Alg@K4. (d) The Langmuir and Freundlich isotherms of Fe/Ca-Alg@K4 beads for CTC adsorption at temperatures of 298, 308, 318, and 328 K.

**Table 3**
Kinetic model parameters for CTC adsorption on Fe/Ca-Alg@K4 beads.

| Kinetic models | Parameter | Fe/Ca-Alg@K4 | |
|---|---|---|---|
| | Initial CTC concentration | 25 mg/L | 50 mg/L |
| PFO | $Q_{e(exp)}$ (mg/g) | 49.68 | 99.84 |
| | $Q_{e(cal)}$ (mg/g) | 48.60 | 97.48 |
| | $K_1$ (1/min) | 0.0368 | 0.0192 |
| | $R^2$ | 0.982 | 0.943 |
| PSO | $Q_{e(cal)}$ (mg/g) | 55.850 | 118.906 |
| | $K_2$ [g/(mg·min)] | $8.255 \times 10^{-4}$ | $1.757 \times 10^{-4}$ |
| | $R^2$ | 0.976 | 0.964 |
| IPD | $K_{id}$ [mg/(g·min ½)] | 3.14937 | 6.67366 |
| | $C$ (mg/g) | 10.620 | 7.116 |
| | $R^2$ | 0.796 | 0.948 |

### 3.1.8. The effect of initial CTC concentration

Fig. 5c indicates that adsorption capacity increased with CTC concentration and then reached a plateau at all temperatures (298–328 K). Equilibrium adsorption capacities reached 249.06, 270.94, 317.03, and 286.72 mg/g at 298, 308, 318, and 328 K, respectively. It may be ascribed that adsorption proceeds gradually at lower CTC concentrations, and as the concentration increases, the available adsorption sites approach saturation [45].

### 3.1.9. Isotherm study

To get insight into the CTC adsorption behavior between CTC and Fe/Ca-Alg@K4 beads at given temperatures, Langmuir and Freundlich isotherm models (nonlinear forms in Table S2) modeled experimental data, with results detailed in Table 4 and Fig. 5d. According to the Langmuir model, the adsorption process occurs on a surface that is uniform, with adsorbate molecules forming a single layer distribution over the adsorbent [46]. The Freundlich model is an empirical equation based on heterogeneous surface adsorption with different affinity binding sites [47].

The high $R^2$ value indicates a good fit between the experimental data and the linear Langmuir model (Table 4). This finding clearly indicated that the adsorption process of CTC onto Fe/Ca-Alg@K4 predominantly involved monolayer adsorption. Additionally, based on the Langmuir model, the maximum adsorption capacity at 318 K was estimated to be 527.32 mg/g. Interestingly, the values of $1/n$ (<1) and $R_L$ (ranging between 0 and 1), as derived from Eq. (9), indicated that the adsorption of CTC onto Fe/Ca-Alg@K4 beads was favorable [47].

$$R_L = \frac{1}{1 + C_0 K_L} \tag{9}$$

## 3.2. Characterization

### 3.2.1. SEM

The surface morphologies of beads (Fig. 6), providing insights into their structural differences. The SEM images of the dried Fe/Ca-Alg@K4 (Fig. 6a) exhibited a spherical shape with diameters ranging from 1.0 to 1.5 mm, 1/3 of wet beads approximately. The cross-sectional analysis (Fig. 6b) revealed a porous interior matrix, indicating favorable conditions for drug encapsulation and controlled release [48]. The presence of K led to the aggregation and flaky morphology of the beads [49]. The surfaces were smooth and opaque (Fig. 6a), while upon the introduction of CTC to Fe/Ca-Alg@K4 (Fig. 6c), the bead surfaces became rough [4,50]. The surface of the spheres was consisted of polyhedral particles of various sizes, forming an uneven structure that closely resembled the ones documented in prior research studies [19]. Moreover, following the adsorption process, SEM images displayed that more cracks appeared on the surface of the beads (Fig. 6d). The surface of the Fe/Ca-Alg@K4@CTC material (Fig. 6d) compared to Fe/Ca-Alg@K4 (Fig. 6b), was filled with numerous fine particles, and the pores on the surface were also filled, resulting in a denser structure. This change may be attributed to CTC adsorption onto bead surfaces induces localized supersaturation, potentially affecting drug diffusion kinetics [19]. Furthermore, freeze-dried beads with varying SA formulations were investigated. Since drug loading was performed using hydrated beads and drug release occurs after the dry beads swell into a hydrated state upon rehydration, the hydrated beads were directly freeze-dried. Their internal pore structures were then characterized *via* SEM imaging to better investigate the effect of pore size on both the adsorption and release of CTC. As shown in Fig. 6 e–g, the SA concentration directly influenced bead morphology, which lower concentrations yielded larger, irregular pores, while higher concentrations produced smaller, more uniform pores. Our study indicated that SA concentration did not affect the drug loading capacity, this suggests that loading behavior is influenced not merely by pore size but also by the molecular interactions between SA and CTC. Excessively larger pores may lead to an initial burst release of the drug, while smaller pores help enhance drug retention capacity, thereby delaying CTC release and achieving more sustainable antibacterial efficacy.

### 3.2.2. EDS analysis

The elemental composition of Fe/Ca-Alg@K4 beads, along with the corresponding elemental mappings, is depicted in Fig. 7a. The presence of carbon and oxygen supports the structural stability of the alginate network, while the identification of aluminum (Al) and silicon (Si) indicates the incorporation of kaolin. Additionally, calcium (Ca) and iron (Fe) suggest the occurrence of cross-linking within the structure [51]. The percentage of Fe was higher than that of Ca, indicating that Fe forms a stronger crosslinking than Ca [52]. Fig. 7b and c show the beads before and after the adsorption of CTC by Fe/Ca-Alg@K4, respectively. The significant increase in the C peak (from 27.4 % to 37.5 %) and the N peak (from 1.01 % to 1.95 %) confirms the successful adsorption of CTC onto the Fe/Ca-Alg@K4 beads [53]. The atomic percentages of Fe and Ca in Fig. 7b are slightly lower than those in Fig. 7c. The observed difference may arise from the interaction between Fe, Ca, and CTC during the adsorption process, such as ion exchange, as well as the decrease in elemental content caused by the adsorbed CTC [19,48]. Additionally, this interaction can alter the elemental composition and distribution within the beads.

### 3.2.3. FTIR analysis

For in-depth insight into prepared beads and CTC adsorption

**Table 4**
Isotherm model parameters of CTC adsorption on Fe/Ca-Alg@K4.

| Isotherm models | Parameter | Fe/Ca-Alg@K4 | | | |
|---|---|---|---|---|---|
| Langmuir | | 298 K | 308 K | 318 K | 328 K |
| | $Q_{e(exp)}$ (mg/g) | 249.06 | 270.94 | 317.03 | 286.72 |
| | $Q_{e(cal)}$ (mg/g) | 344.39 | 466.62 | 527.32 | 487.02 |
| | $K_L$ (L/mg) | 0.0313 | 0.0287 | 0.0240 | 0.0171 |
| | $R^2$ | 0.749 | 0.951 | 0.808 | 0.938 |
| | $R_L$ | 0.137–0.761 | 0.148–0.777 | 0.137–0.761 | 0.225–0.853 |
| Freundlich | $1/n$ | 0.505 | 0.555 | 0.622 | 0.665 |
| | $K_F$ (mg/g) (L/mg)$^n$ | 26.952 | 29.296 | 24.736 | 15.895 |
| | $R^2$ | 0.687 | 0.881 | 0.767 | 0.918 |

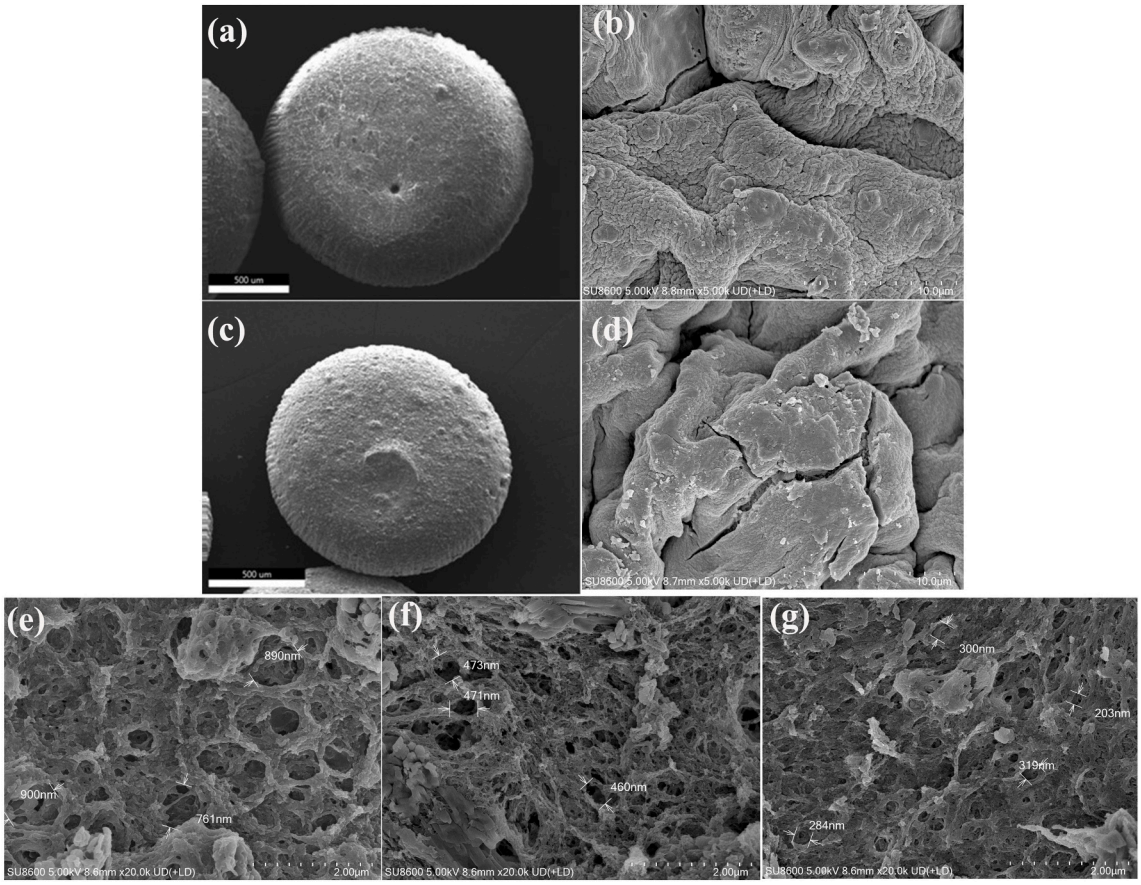


**Fig. 6.** SEM images of Fe/Ca-Alg@K4 (a–b) and Fe/Ca-Alg@K4@CTC (c–d). SEM images of freeze-dried of Fe/Ca-Alg@K (e), Fe/Ca-Alg@K3 (f) and Fe/Ca-Alg@K4 (g).

interactions, FTIR was conducted. In Fig. 8a, the stretching vibration of OH group appears at 3410.26 $cm^{-1}$, and CH stretching is noted at 2924.18 $cm^{-1}$ in the FTIR spectrum of SA [49]. Kaolin exhibited O—H stretching vibrations at 3626.29 $cm^{-1}$ and 3487.42 $cm^{-1}$ due to hydroxyl groups grafted onto aluminum sites [24], while its Si—O and Si—O—Si vibrations appeared at 1635.69 $cm^{-1}$ and 1026.16 $cm^{-1}$ [54], respectively. Additionally, Al—OH bending vibrations and Al—O—Si bending vibrations were observed at 933.58 $cm^{-1}$ and 540 $cm^{-1}$ [49,55]. The FTIR spectrum of Fe/Ca-Alg@K beads retained the FTIR bands of both SA and K, demonstrating consistency between these two materials. However, some peaks exhibited wavenumber shifts. Notably, the asymmetric stretching vibration of the carboxylate group shifted to higher wavenumbers (1643.41 $cm^{-1}$) in Fe/Ca-Alg@K composite beads compared to its position in SA (1620.26 $cm^{-1}$), attributable to K incorporation, suggesting potential interactions between the components. From the FTIR spectra of Fe/Ca-Alg@K, Fe/Ca-Alg@K3, and Fe/Ca-Alg@K4 in Fig. 8b, it was observed that as the concentration of SA increased, the intensity decreased. This may originate from the increased formation of coordination bonds between carboxyl groups ($—COO^-$) in high concentration SA and $Al^{3+}$/$Si^{4+}$ in K, along with the resulting dense network formation, and coupled with the restriction on molecular chain vibrational freedom imposed by hydrogen-bonding networks between —OH/$—COO^-$ groups of SA and surface —OH groups of K. As shown in Fig. 8c, the primary FTIR bands of the Fe/Ca-Alg@K4@CTC beads were retained with wavenumber shifts, confirming the adsorption of CTC onto Fe/Ca-Alg@K4. Characteristic peaks at 2851.20 $cm^{-1}$ and 1458.28 $cm^{-1}$ were attributed to $CH_3$ group stretching vibrations [56] and skeletal vibrations in the aromatic ring of CTC, respectively, similar to previous studies [57].

### 3.2.4. XPS analysis

The XPS spectra of Fe/Ca-Alg@K4 beads before and after adsorption are shown in Fig. 9. The survey scan spectra of Fe/Ca-Alg@K4 beads in Fig. 9a reveal that the primary elements of the Fe/Ca-Alg@K4 beads are C, O, Al, Si, N, Fe, and *Ca.* The characteristic N 1s peak in Fe/Ca-Alg@K4 beads after CTC adsorption was raised from 1.01 to1.83 %, providing crucial evidence for the adsorption of CTC molecules onto the adsorbent. Moreover, the enhancement of the C element and the weakening of the Fe and Ca elements were consistent with those observed in previous EDS results, indicating an interaction between Fe/Ca-Alg@K4 and CTC.

Fig. 9b displays the high-resolution C 1s XPS spectrum of the bead before and after CTC adsorption. The spectrum can be split into three peaks at binding energies of 288.39–288.41 eV, 286.38–286.41 eV, and 284.56–284.59 eV, corresponding to C═O, C—O—C, and C—C/C—H groups, respectively [58]. These changes are attributed to an electron cloud shift between the Fe/Ca-Alg@K4 beads and CTC molecules, indicating the involvement of these active functional groups in the adsorption process [56]. The O 1s peaks of Fe/Ca-Alg@K4 illustrated in Fig. 9c at 530.97, 532.0, 532.95, and 533.09 eV could be assigned to Al—O or Al—OH, C═O, $SiO_2$, and C—O or OH bond, respectively [59,60]. After CTC adsorption, all the decomposed O 1s peaks exhibited a shift in position. This is probably because the oxygen - containing functional groups (such as —COOH and OH) on the Fe/Ca-Alg@K4 beads react with the benzene rings and highly electronegative atoms within CTC molecules. This interaction likely occurred through n-π EDA interactions and hydrogen bonding during the adsorption process [56,61]. Additionally, the peak for the —OH stretching vibration shifted from 3448.84 $cm^{-1}$ to 3479.70 $cm^{-1}$, confirming the existence of hydrogen bonding [59].

In Fig. 9d, the N 1s peak, with a low proportion of only 1.01 % at

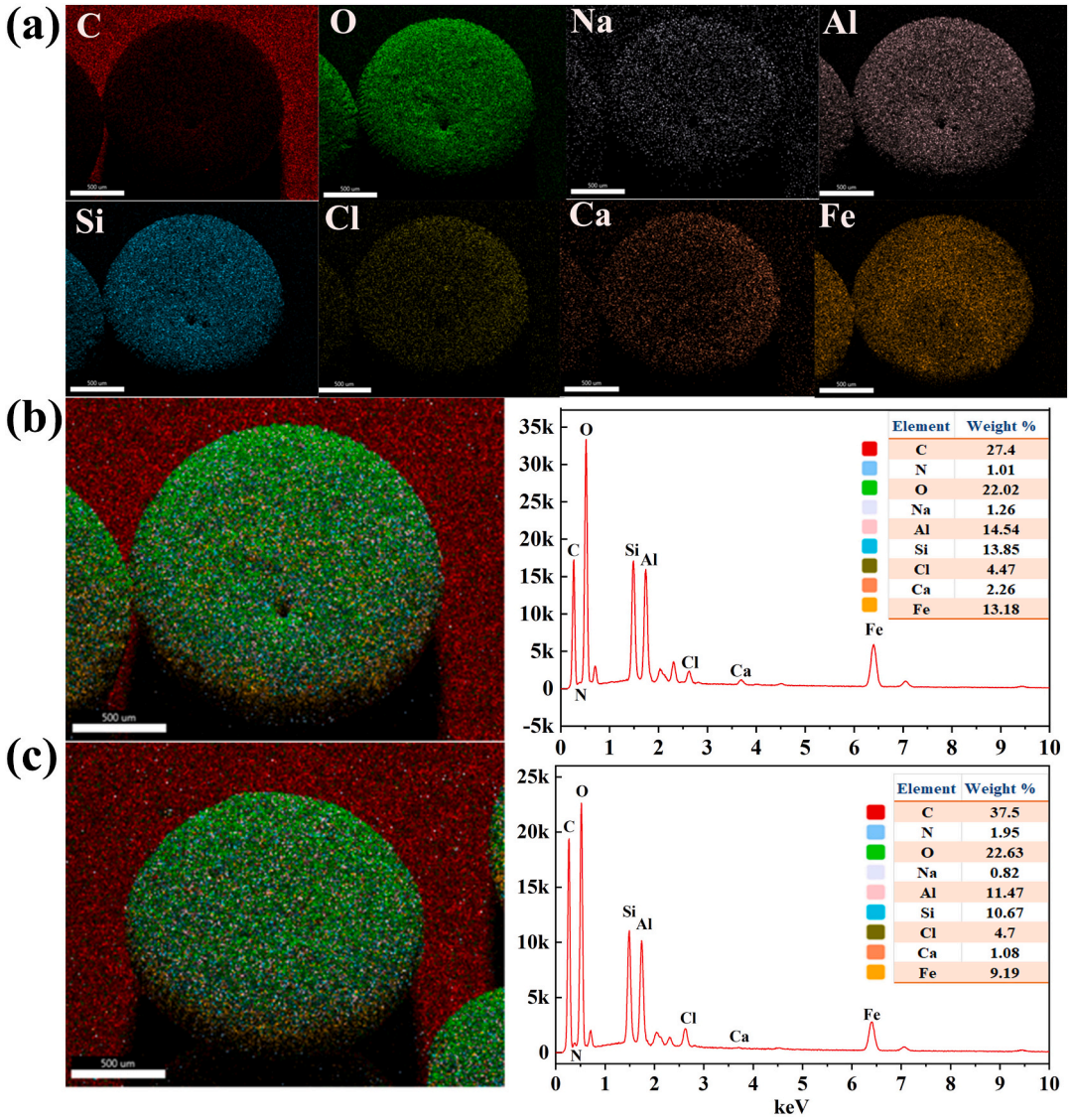


**Fig. 7.** (a) EDS mappings of C, O, Na, Al, Si, Cl, Ca, and Fe on Fe/Ca-Alg@K4 beads, and (b) EDS spectra of Fe/Ca-Alg@K4 beads before and (c) after CTC adsorption.

400.12 eV, is initially attributed to $NSiO_2$ in K [62]. Following CTC adsorption, the observed shift in binding energy and increase in peak area suggest that, in addition to $NSiO_2$, new species such as —NH or —CO—NH— groups are present [61]. Meanwhile, the emergence of new peaks at 401.52 eV and 402.73 eV, corresponding to tertiary amine ($N^+$) and —N—O respectively, following CTC adsorption, indicates the successful adsorption of CTC onto Fe/Ca-Alg@K4 beads. This also underscored the crucial role played by amino groups and the electrostatic interactions between $N^+$ and the beads throughout the adsorption process [61,62].

Furthermore, after CTC adsorption, the existence of aluminosilicate groups was confirmed by the Al 2p peak at 74.57 eV and Si 2p at 102.9 eV in Fig. 9e and f, demonstrating that K exists in Fe/Ca-Alg@K4 [63]. The shifts in the high-resolution XPS of Al 2p and Si 2p, respectively, suggesting that Al and Si may have participated in the surface complexation with CTC, similar to previous research of ciprofloxacin adsorption onto K [64]. Additionally, Fig. 5g and h revealed significant reductions in the characteristic peaks of Fe 2p and Ca 2p, along with shifts in binding energy to lower values, indicating that $Fe^{3+}$ and $Ca^{2+}$ were also involved in the adsorption process. These changed could be attributed to the interaction between $Fe^{3+}$, $Ca^{2+}$ and the O or N atoms in CTC molecules, followed by charge transfer from oxygen or nitrogen to $Fe^{3+}$ and $Ca^{2+}$, resulting in decreased binding energy peaks for Ca 2p and Fe 2p. The hydroxyl, carbonyl, keto and amino groups in CTC molecules provide abundant electrons to $Fe^{3+}$ and $Ca^{2+}$, forming metal complexes with these cations through cation-π bonds, cation-n bridges [56]. In addition, it revealed coordination bonds may also participate between $Fe^{3+}$ and the phenolic hydroxyl/amide groups of CTC.

### 3.2.5. XRD, TGA, and BET analysis

The XRD pattern of K presented in Fig. 10a is consistent with the description in previous literature [65], where the diffraction peaks at 21.51°, 35.27°, 37.84°, 54.19°, and 70.76° correspond to the reflections of the (100), (110), (003), (210), and (220) crystalline planes of K, respectively [65]. Upon examining the XRD pattern of Fe/Ca-Alg@K4, it can be observed that its main diffraction peaks are similar to those of K but with reduced intensity, suggesting that after being compounded with Fe/Ca-Alg, K is not only well-preserved but also uniformly dispersed within the beads.

In the TG curve of Fig. 10b, the thermal decomposition processes of Fe/Ca-Alg@K4, Fe/Ca-Alg@K4@CTC, and Fe/Ca-Alg commence approximately at 70 °C, followed by significant mass loss within the temperature range of 200 to 400 °C. This initial mass loss occurs between 70 and 100 °C was mainly by the evaporation of moisture

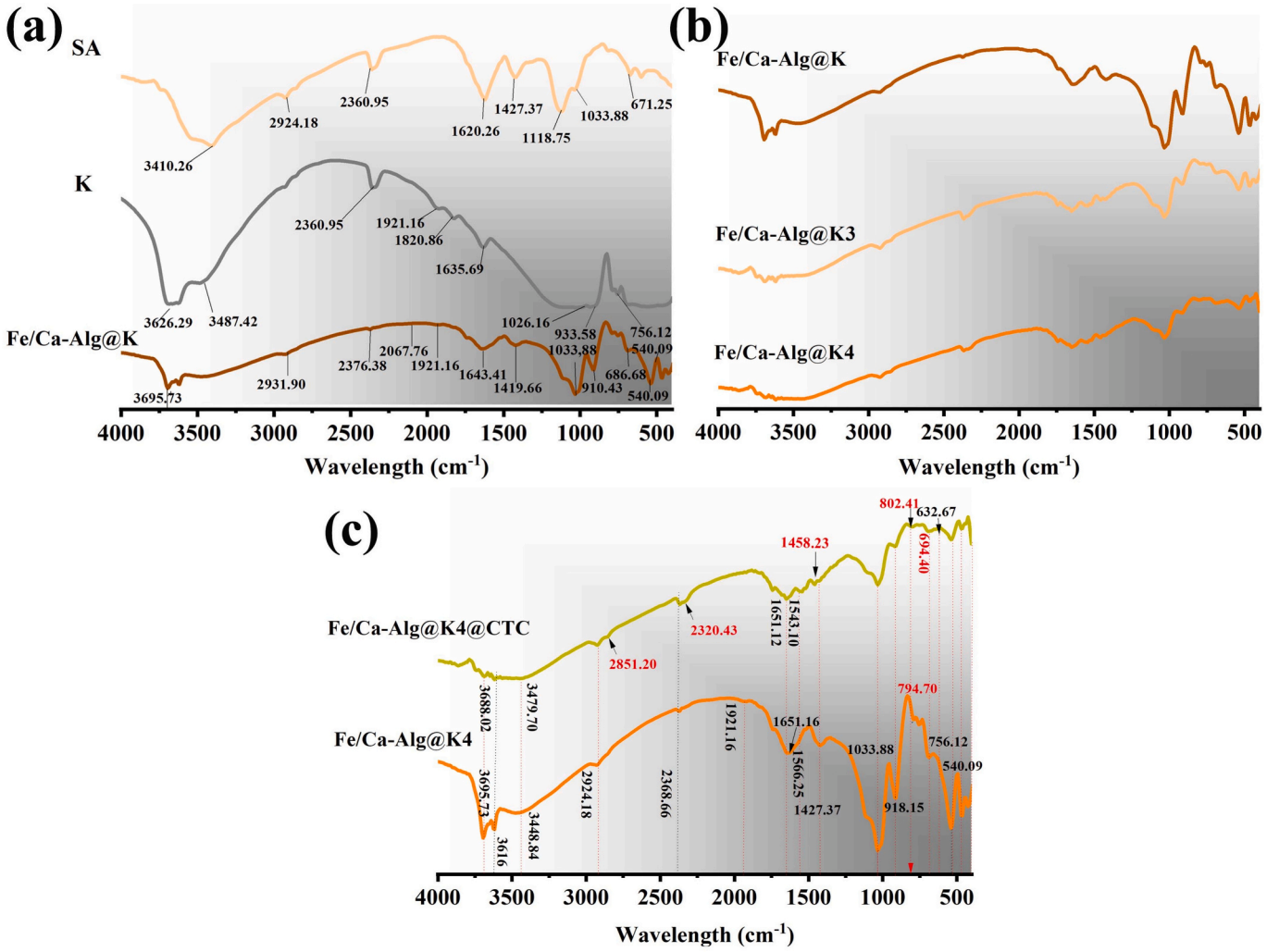


**Fig. 8.** (a) FTIR analysis of SA, K and Fe/Ca-Alg@K4, (b) Fe/Ca-Alg@K, Fe/Ca-Alg@K3, and Fe/Ca-Alg@K4, (c) Fe/Ca-Alg@K4 and Fe/Ca-Alg@K4@CTC.

contained within the beads [66]. Subsequently, the decomposition of SA in beads dominated the process, continuing until the temperature reaches 450 °C, particularly under a $N_2$ atmosphere, the SA in Fe/Ca-Alg@K4 converts to carbon between 200 and 400 °C [3]. When the temperature exceeds 500 °C, the remaining mass is primarily composed of carbon and K [65]. Compared to the Fe/Ca-Alg@K4 beads, Fe/Ca-Alg beads exhibit a faster decomposition rate and a higher decomposition temperature. On the other hand, Fe/Ca-Alg@K4 beads, due to the incorporation of K, effectively enhance their thermal stability through their high thermal stability and interaction with the polymer matrix.

The $N_2$ adsorption/desorption isotherm and the corresponding Barrett–Joyner–Halenda (BJH) pore size distribution for Fe/Ca-Alg@K4 are presented in Fig. 10c and d. The surface area of Fe/Ca-Alg@K4 beads was 4.56 $m^2$/g, which was larger than the measured surface area of alginate beads alone (less than 2.4 $m^2$/g) [50], but lower than that of K alone (9.51 $m^2$/g) [67]. This phenomenon may be attributed to the incorporation of K, which promotes the formation of cracks, thereby increasing the porosity of the alginate beads. Meanwhile, it was aslo noted that compared to K, the beads exhibited a smaller pore volume (0.032 $cm^3$/g, compared to 0.12 $cm^3$/g) and larger pore diameters (28.66 nm, compared to 22.16 nm) [19]. This could be due to the successful integration of K particles into the alginate polymer network. Furthermore, BET analysis revealed an important fact that the high performance of Fe/Ca-Alg@K4 beads in CTC adsorption was not solely determined by their porosity or specific surface area. In fact, the strength of interaction between binding sites and guest species was also a crucial factor in determining their absorption capacity [68]. This finding is consistent with the effect of SA dose on loading capacity and SEM morphology of three prepared formulations.

### 3.3. Interaction mechanism

Fig. 11a illustrates the potential cross-linking mechanism between $Fe^{3+}$/$Ca^{2+}$ and the alginate network, along with their interactions with the surface of the K mineral. $Fe^{3+}$ binds to both guluronate (GG) and mannuronate (GM) groups, while $Ca^{2+}$ specifically binds to GG groups, forming the characteristic egg-box structure [52]. Additionally, alginate may interact with kaolin minerals through hydrogen bonding and electrostatic interactions, enhancing the overall stability and functionality of the composite material [19].

The proposed mechanism of CTC adsorption is illustrated in Fig. 11b. Based on the comprehensive assessment of characterization outcomes, pH effect, adsorption kinetics, and isotherm analyses, the adsorption process of CTC onto Fe/Ca-Alg@K4 beads appears to governed by a complex combination of chemical and physical interactions, along with the surface uniformity of the beads. There may be three potential adsorption sites inside the beads Alg@K cross linked Fe/Ca, including (1) Fe and Ca presented in Fe/Ca-Alg@K4, (2) K captured within the sphere, and (3) SA combined with K minerals. The loading mechanism of CTC can be elucidated as follows, according to BET analysis, Fe/Ca-Alg@K4 beads exhibit a substantial specific surface area and pore size. These facilitated the diffusion of CTC within the pores of the beads,

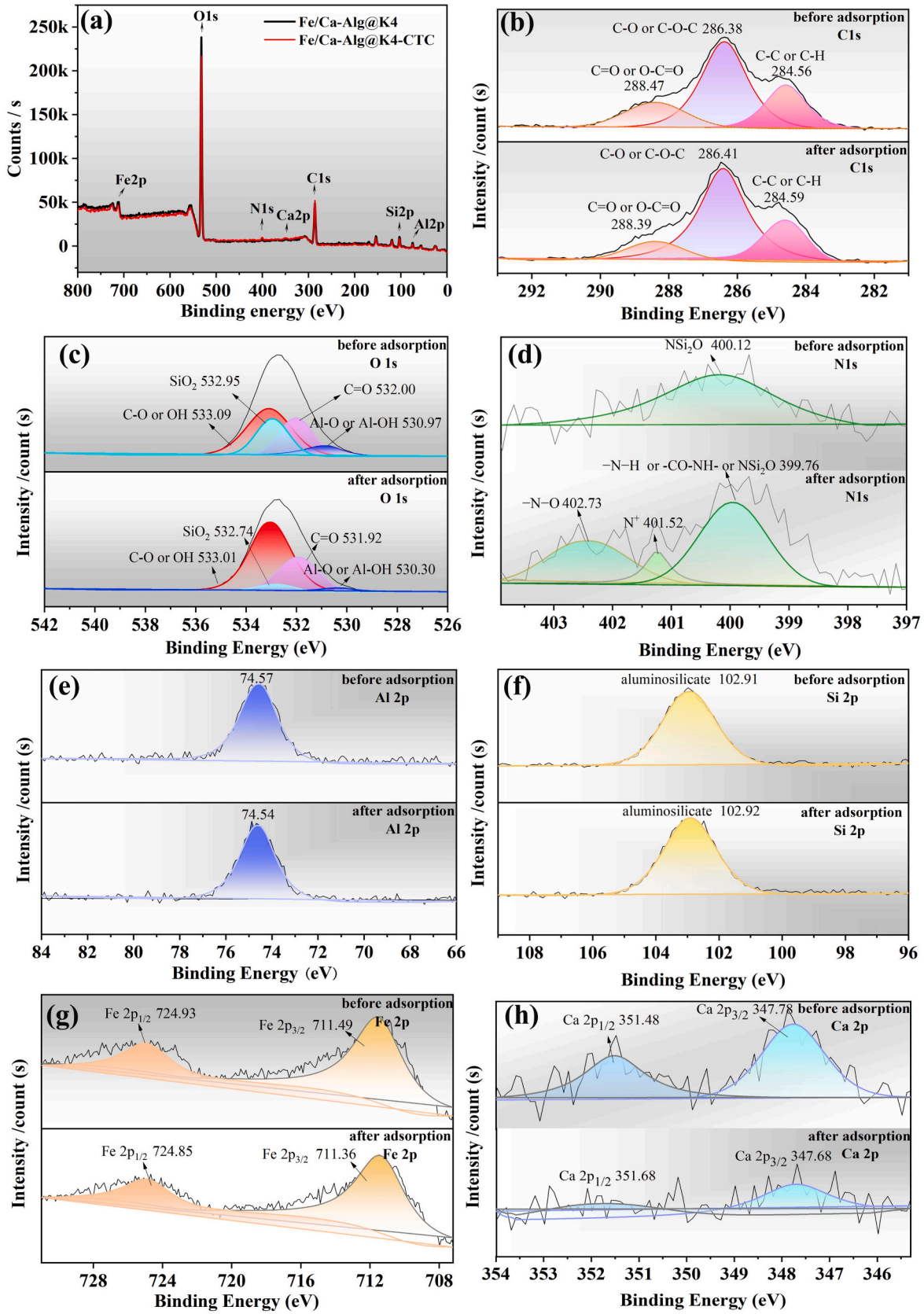


**Fig. 9.** XPS survey scan spectra of Fe/Ca-Alg@K4 beads and Fe/Ca-Alg@K4@CTC.

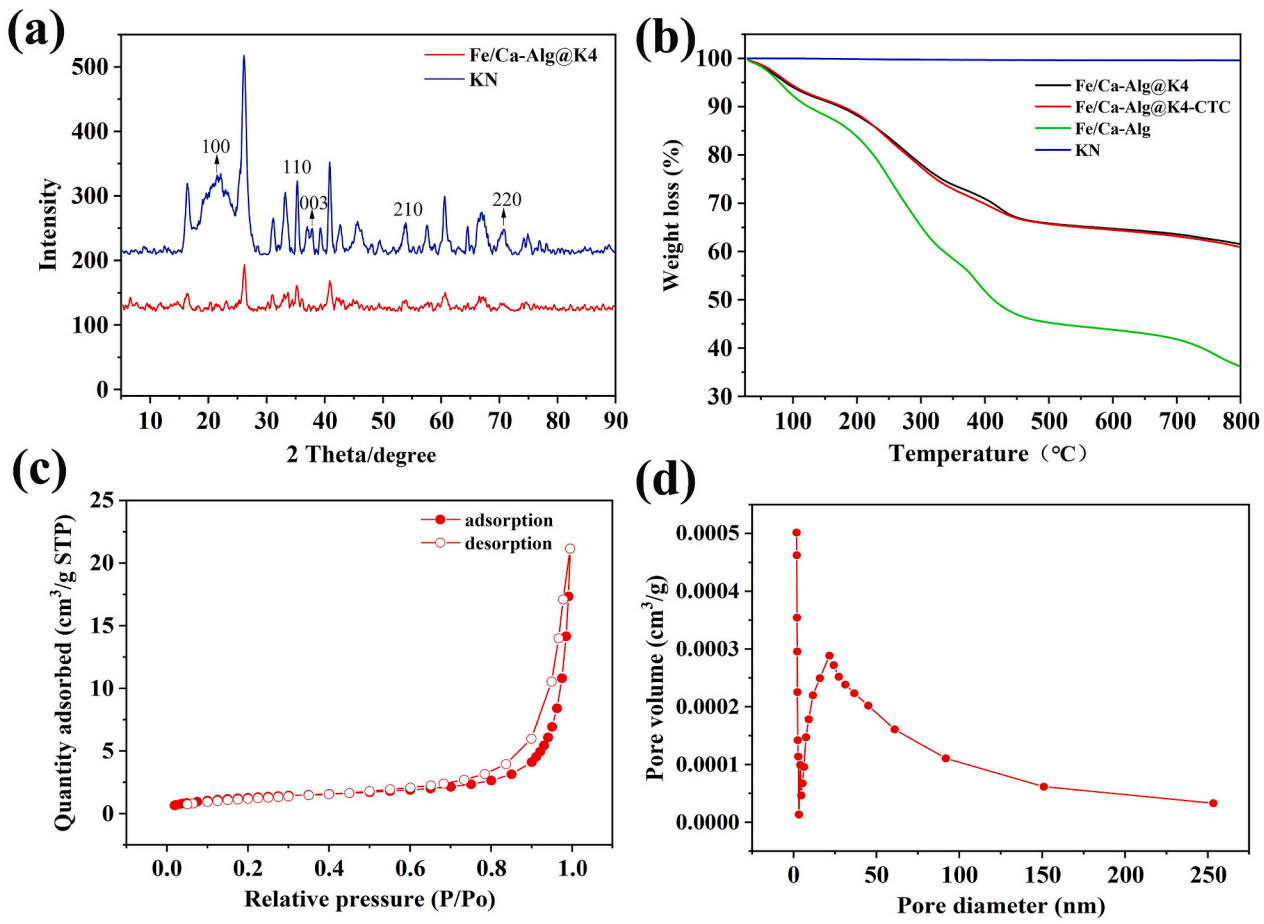


**Fig. 10.** (a) The XRD patterns of Fe/Ca-Alg@K4 and K, (b) TGA of Fe/Ca-Alg@K4, Fe/Ca-Alg@K4-CTC, Fe/Ca-Alg, and K performed under air atmosphere, (c) $N_2$ adsorption/desorption isotherm of Fe/Ca-Alg@K4 at 77 K, and (d) pore size distribution of Fe/Ca-Alg@K4.

thereby enhancing its encapsulation efficiency. Furthermore, several interaction mechanisms contribute to this loading. Strong n-π EDA interactions occur between the Al—OH or sodium alginate—OH (SA—OH) groups and the benzene ring of CTC. Cation-n bridges, involving interactions between $Fe^{3+}$/$Ca^{2+}$/$Al^{3+}$/$Si^{4+}$ and the electron-rich O and N atoms in SA and CTC. Additionally, hydrogen bonding formed between the active oxygen-containing functional groups on the Fe/Ca-Alg@K4 beads and CTC molecules further contributes to CTC loading. Cation-π interactions between $Fe^{3+}$/$Ca^{2+}$/$Al^{3+}$/$Si^{4+}$ and benzene ring in CTC also play a role. Lastly, surface complexation, electrostatic interactions and cation ion exchange between cationic CTC molecules and Fe/Ca-Alg@K4 beads further facilitate the loading process [69].

### 3.4. *In vitro release study of CTC*

The release profiles of CTC from K, Fe/Ca-Alg@K, Fe/Ca-Alg@K3, and Fe/Ca-Alg@K4 beads were evaluated under simulated physiological conditions (pH 1.2 and pH 7.4, 37 °C, Fig. 12a, b). All formulations exhibited sustained-release characteristics, with the cumulative release following the consistent order, Fe/Ca-Alg@K4 < Fe/Ca-Alg@K3 < Fe/Ca-Alg@K < K. Both the synthesized beads and K alone exhibit a sustained-release ability, likely attributed to multiple interaction forces with CTC, which stabilize the drug molecules within the matrix. Notably, the K achieved 100 % release within 24 h under pH 1.2. This rapid release from K may be attributed to its inherent hydrophilicity, good solubility of CTC in acidic pH, and the electrostatic repulsion between positively charged K matrix and protonated CTC molecules under acidic conditions (pH 1.2), which collectively accelerated drug diffusion. Similar behavior was observed with hallosyite nanotubes loaded norfloxacin [27]. At pH 7.4, K release was moderately slower, while the difference was minor, as both diffusion and electrostatic repulsion between $K^-$ and $CTCH^-$ ions remained operative.

Fig. 12c shows that CTC release from all beads was higher at pH 1.2 within the first 0.75 h, but this trend reversed after prolonged incubation, with release at pH 7.4 surpassing that at pH 1.2. Fe/Ca-Alg@K4 released nearly 100 % of CTC after 73 h at pH 7.4 (Fig. 12b), compared to only ~70 % at pH 1.2 (Fig. 12a). The phenomenon could be explained by alginate hydrogel swelling behavior and low solubility of CTC in neutral pH. The beads exhibit more obvious swelling at pH 7.4 (Fig. 12d). In initial phase of pH 1.2 (0–0.75 h), carboxyl protonation (—COOH) occurs, causing hydrogel shrinkage, exhibits an extremely low swelling degree [70], then allowing drugs diffuse directly through the pores. Additionally, protonation of $CTC^{3+}$ generates electrostatic repulsion and $H^+$ ions may disrupt the $Fe^{3+}$/$Ca^{2+}$ cross-linking structure also accelerated CTC release. Conversely, at pH 7.4, ionization of carboxyl groups (—$COO^-$) triggers charge repulsion, and the dried hydrogel beads undergoes a time-consuming water absorption and swelling process to achieve swelling equilibrium overcome the hydrogen bonding between molecular chains, impeding initial diffusion pathways. However, the subsequent increase in cumulative release at pH 7.4 stems from the completion of swelling after 0.75 h, which forms water channels enabling CTC continuous diffusion. Furthermore, sustained swelling also enables phosphate ions ($PO_4^{3-}$) in the buffer to react with $Fe^{3+}$ and $Ca^{2+}$, ultimately disrupting the gel network structure of the beads to increase drug release [71,72]. In contrast, the hydrogel structure in the acidic environment becomes increasingly dense over time, thereby inhibiting the sustained release of drugs.

Thus, the pH-dependent release kinetics, characterized by a low

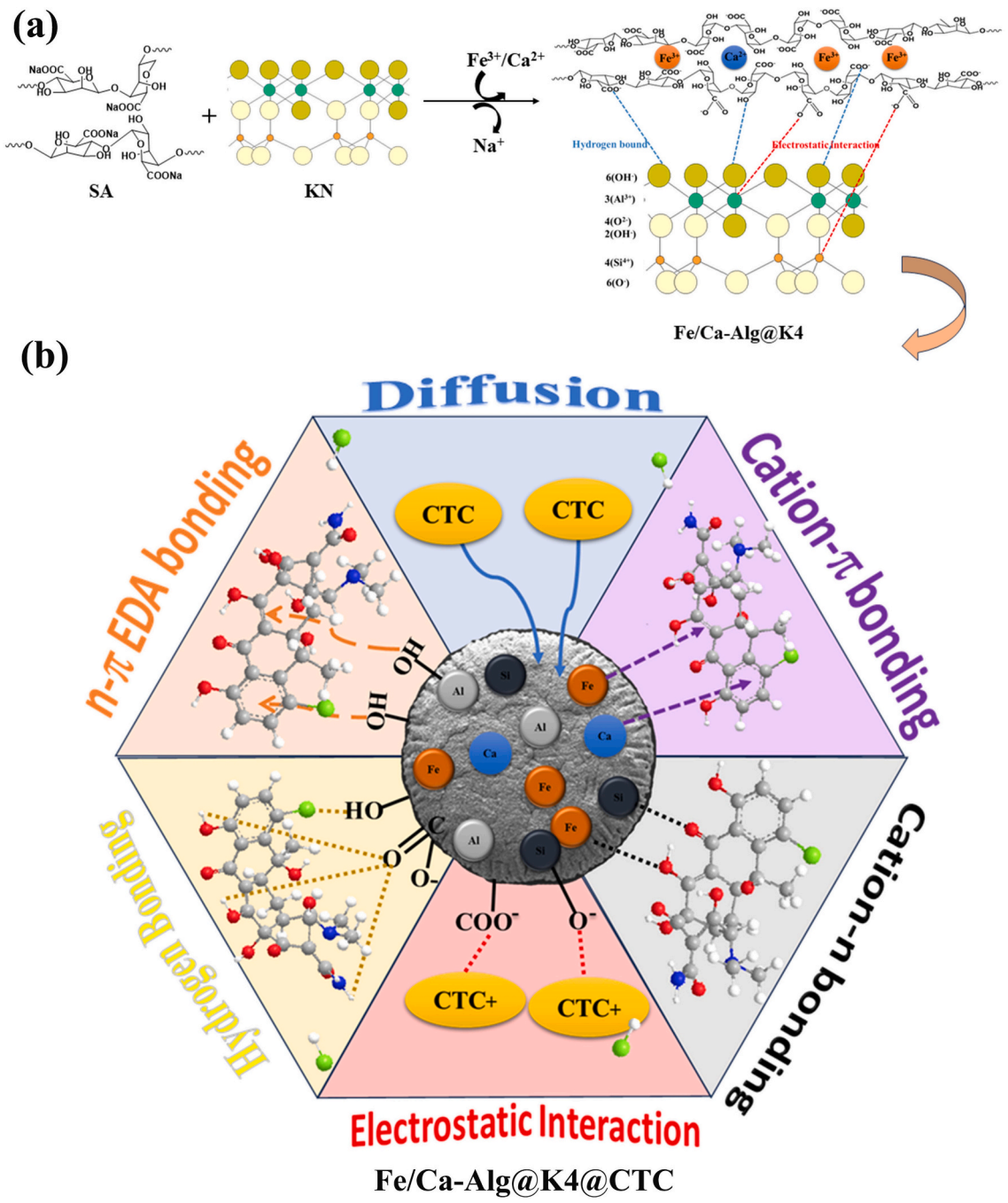


**Fig. 11.** (a) A formation mechanism of Fe/Ca-Alg@K4 beads and (b) the mechanism of interaction between CTC and Fe/Ca-Alg@K4 beads.

cumulative release at pH 7.4 within the initial 2 h and complete release over a prolonged period, are highly beneficial. This targeted release profile is designed to coincide with the physiological pH of the intestinal tract, the primary site for CTC absorption. By minimizing premature release in the acidic stomach and ensuring maximal release in the intestines, this system significantly enhances the oral bioavailability and therapeutic efficacy of CTC [73].

Notably, the concentration of SA exerts a significantly modulated CTC release under both pH conditions (Fig. 12a, b), with higher SA concentrations reducing drug release. However, the underlying mechanisms differ with pH. At pH 1.2, there are no significant differences in swelling among beads with different concentrations of SA ($p > 0.05$, Fig. 12e), it is not the primary factor contributing to the differences in release behavior. The release differences mainly stem from two aspects. Firstly, higher SA concentration resulted in reduced drug release, likely due to increased restrictions on intraparticle diffusion and the reduction in the approachable free volume (low water adsorption) of water molecules in more dense alginate hydrogel beads [22]. Furthermore, molecular interactions between SA and CTC, such as cation-π, cation-n, n-π interactions, hydrogen bonding, and electrostatic forces were contributed to the decelerated release kinetics [22]. At pH 7.4, a significant difference in swelling was observed among the three beads ($p < 0.001$, Fig. 12e), all of which exhibited high swelling efficiency. This swelling behavior is likely the dominant factor causing the variation in release rates. Among them, Fe/Ca-Alg@K, which had the fastest release rate, can be attributed to its highest degree of swelling, which enables it to rapidly absorb water and form larger pores [74]. These results indicate that the system possesses pH-responsive and tunable release properties.

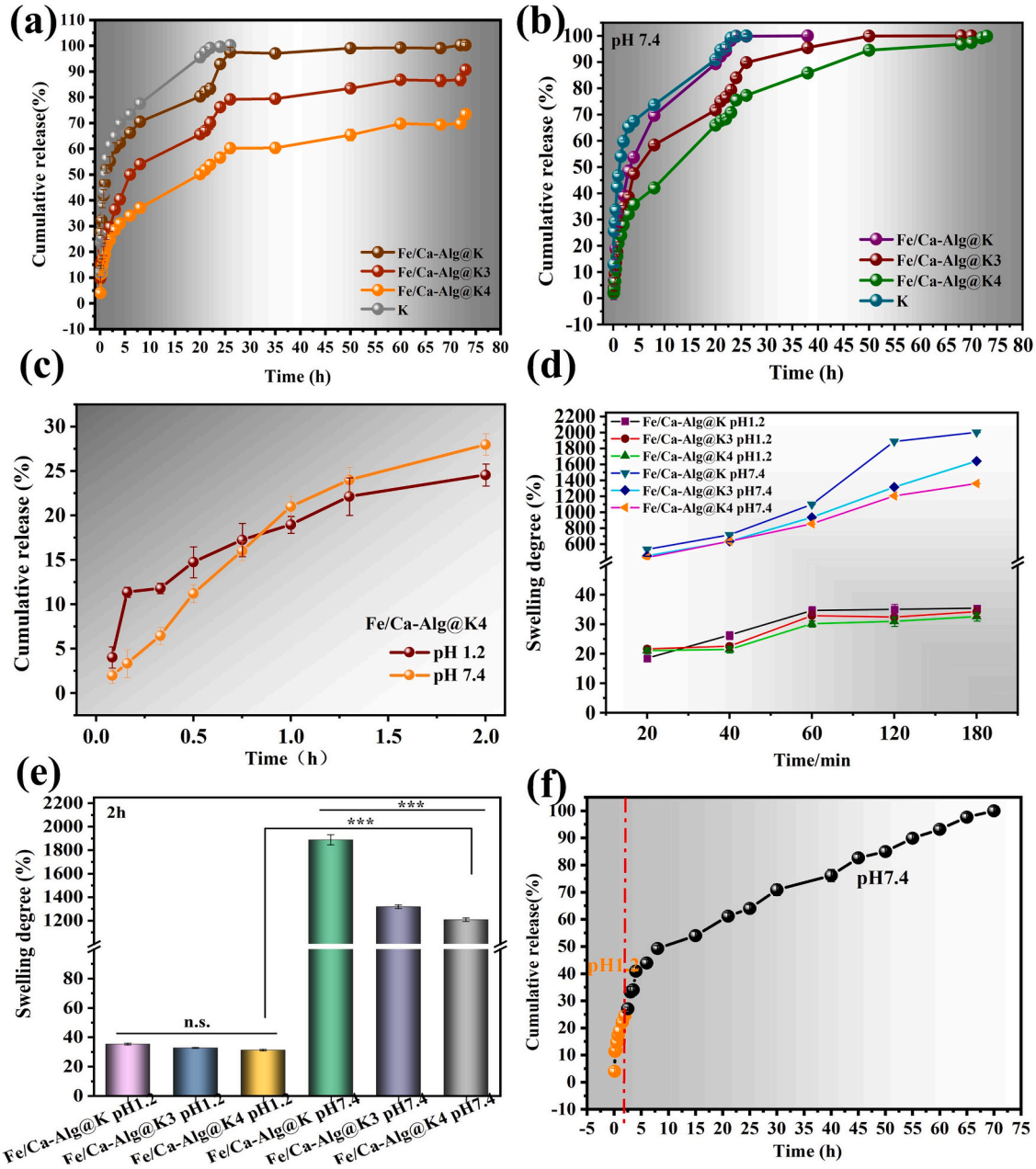


**Fig. 12.** (a) and (b) are the CTC release profiles from K, Fe/Ca-Alg@K, Fe/Ca-Alg@K3, and Fe/Ca-Alg@K4 at pH 1.2 and pH 7.4 *in vitro*, respectively. (c) CTC cumulative release curve from Fe/Ca-Alg@K4 at pH 1.2 and pH 7.4 in initial 2 h. (d) and (e) are the swelling degree curves and comparative swelling data at 2 h after CTC adsorption at pH 1.2 and 7.4 for Fe/Ca-Alg@K, Fe/Ca-Alg@K3, and Fe/Ca-Alg@K4, respectively. (f) Release kinetics of CTC from Fe/Ca-Alg@K4 under simulated oral conditions.

Additionally, *in vitro* experiments were conducted to investigate the release kinetics of CTC from Fe/Ca-Alg@K beads under conditions simulating the human oral route. The Fe/Ca-Alg@K4@CTC beads were initially placed in a simulated gastric medium for 2 h and then transferred to a simulated intestinal medium for 70 h. *In vitro* drug release studies indicated that approximately 26 % of CTC was released from Fe/Ca-Alg@K4 within the first 2 h at pH 1.2. Following this, the beads disintegrated and gradually released the remaining drug in the simulated intestinal environment (pH 7.4) over the next 70 h (Fig. 12f).

### 3.5. Kinetic measurements of drug release

To elucidate the release mechanisms, *in vitro* data were fitted to four kinetic models (Fig. 13). As summarized in Table 5, the Korsmeyer-Peppas (Kors-Peppas) model showed the highest correlation coefficients ($R^2$) for all formulations in pH 1.2. And the release exponent ($n$) values for the three beads and K were below 0.5, indicating quasi-Fickian diffusion dominated by concentration gradients. In contrast, at pH 7.4, Higuchi and Kors-Peppas model all show high $R^2$ for beads and K. Notably, the Higuchi model achieved higher $R^2$ values for the three different formulations beads, which indicates diffusion is the dominant. However, the $n$ values were 0.522, 0.517 and 0.514 (ranged between 0.5 and 1.0) for Fe/Ca-Alg@K, Fe/Ca-Alg@K3 and Fe/Ca-Alg@K4, respectively, signifying non-Fickian diffusion where drug release was jointly controlled by diffusion, polymer swelling and erosion [75]. The most obvious anomalous diffusion in Fe/Ca-Alg@K (highest $n$ value) presumably correlates with its enhanced swelling capacity. These release modeling outcomes under both pH conditions strongly well-aligned with

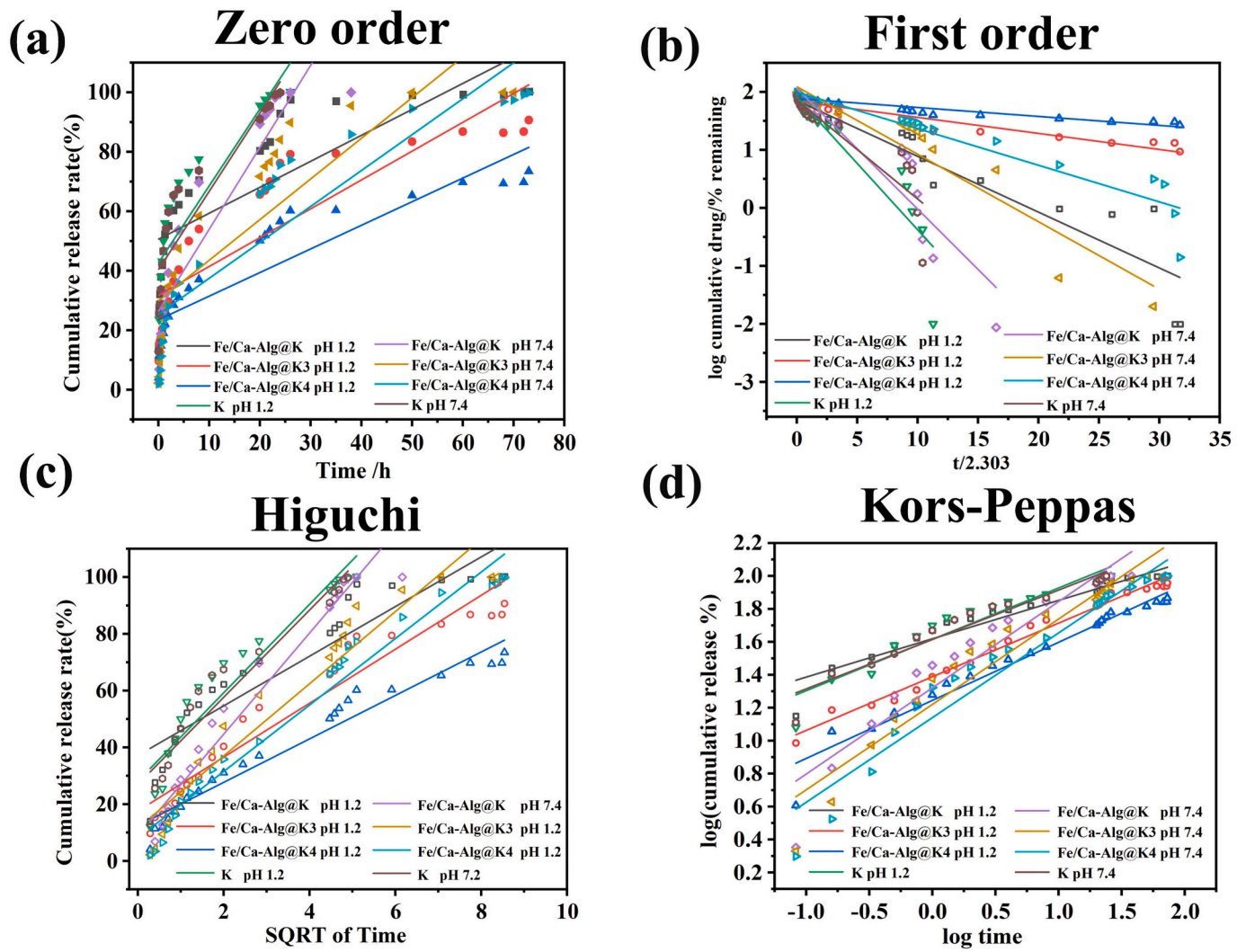


**Fig. 13.** *In vitro* CTC release data for various beads and K. (a) Zero-order model, (b) First-order model, (c) Higuchi model, and (d) Kors-Peppasmodel.

**Table 5**
*In vitro* CTC release data for prepared beads and K.

| pH | Materials | Zero-order | | First-order | | Higuchi | | Korsmeyer-Peppas | | |
|---|---|---|---|---|---|---|---|---|---|---|
| | | $K_0$ | $R_1^2$ | $K_1$ | $R_2^2$ | $K_H$ | $R_3^2$ | $K_{KP}$ | $n$ | $R_4^2$ |
| 1.2 | Fe/Ca-Alg@K | 0.873 | 0.678 | 0.0962 | 0.890 | 8.744 | 0.863 | 41.495 | 0.233 | 0.929 |
| | Fe/Ca-Alg@K3 | 0.970 | 0.761 | 0.0277 | 0.914 | 9.501 | 0.929 | 24.434 | 0.326 | 0.985 |
| | Fe/Ca-Alg@K4 | 0.794 | 0.808 | 0.0154 | 0.903 | 7.656 | 0.954 | 17.539 | 0.353 | 0.956 |
| | K | 2.588 | 0.774 | 0.2287 | 0.847 | 15.578 | 0.902 | 41.210 | 0.312 | 0.922 |
| 7.4 | Fe/Ca-Alg@K | 2.756 | 0.884 | 0.208 | 0.881 | 17.776 | 0.957 | 21.028 | 0.522 | 0.914 |
| | Fe/Ca-Alg@K3 | 1.570 | 0.757 | 0.116 | 0.902 | 12.697 | 0.927 | 16.680 | 0.517 | 0.926 |
| | Fe/Ca-Alg@K4 | 1.208 | 0.821 | 0.0631 | 0.911 | 11.706 | 0.964 | 13.770 | 0.514 | 0.943 |
| | K | 2.631 | 0.815 | 0.170 | 0.809 | 15.309 | 0.919 | 41.257 | 0.299 | 0.936 |

the observed pH-dependent swelling behavior [4].

The $n$ value of K remained below 0.5 under pH 7.4 conditions, indicating that its release was not affected by effects such as swelling and was dominated by diffusion as the primary mechanism, resulting in a relatively rapid release rate. This result indirectly confirms that the combination of SA and K can significantly optimize the sustained release effect. The hydrogel network formed by SA prolongs the drug release rate by regulating swelling behavior and diffusion resistance, overcoming the drawback of excessively rapid release from pure K, and thereby improving the bioavailability of CTC.

### 3.6. Antibacterial activity

The agar diffusion test was employed to evaluate the performance of the beads and kaolin against Gram-negative (*E. coli*) and Gram-positive (*S. aureus*). *E. coli* is a common pathogen associated with gastrointestinal and urinary tract infections, while *S. aureus* is known for producing enterotoxins responsible for food poisoning [76]. After 24 h of incubation, K encapsulated with CTC (K@CTC) and K-based SA beads encapsulated with CTC, namely Fe/Ca-Alg@K@CTC, Fe/Ca-Alg@K3@CTC, and Fe/Ca-Alg@K4@CTC, shown significant antibacterial efficacy against both *E. coli* and *S. aureus*. The size of the inhibition zone was

influenced by the concentration of SA (Fig. 14a, b). Higher concentrations resulted in smaller inhibition zones, which may be related to the modulation of drug release behavior. Among all formulations, the Fe/Ca-Alg@K@CTC exhibited the largest inhibition zones, measuring 31.6 mm against *E. coli* and 24.8 mm against *S. aureus*. This outstanding performance may be attributed to their sustained and rapid release of CTC, further demonstrating that SA concentration regulates antimicrobial efficacy. The inverse relationship between SA and inhibition zone size suggests that the denser network structure of beads with higher SA content decreases the diffusion and release of CTC, thereby regulating the extent of antibacterial activity. This sustained-release characteristic could offer particular advantages for applications requiring long-term antimicrobial protection.

The beads maintained potent antibacterial activity against *E. coli* and *S. aureus* even 4 h after CTC release (Fig. 14c and d), due to their strong capacity to retain the drug within their matrix. Although the beads

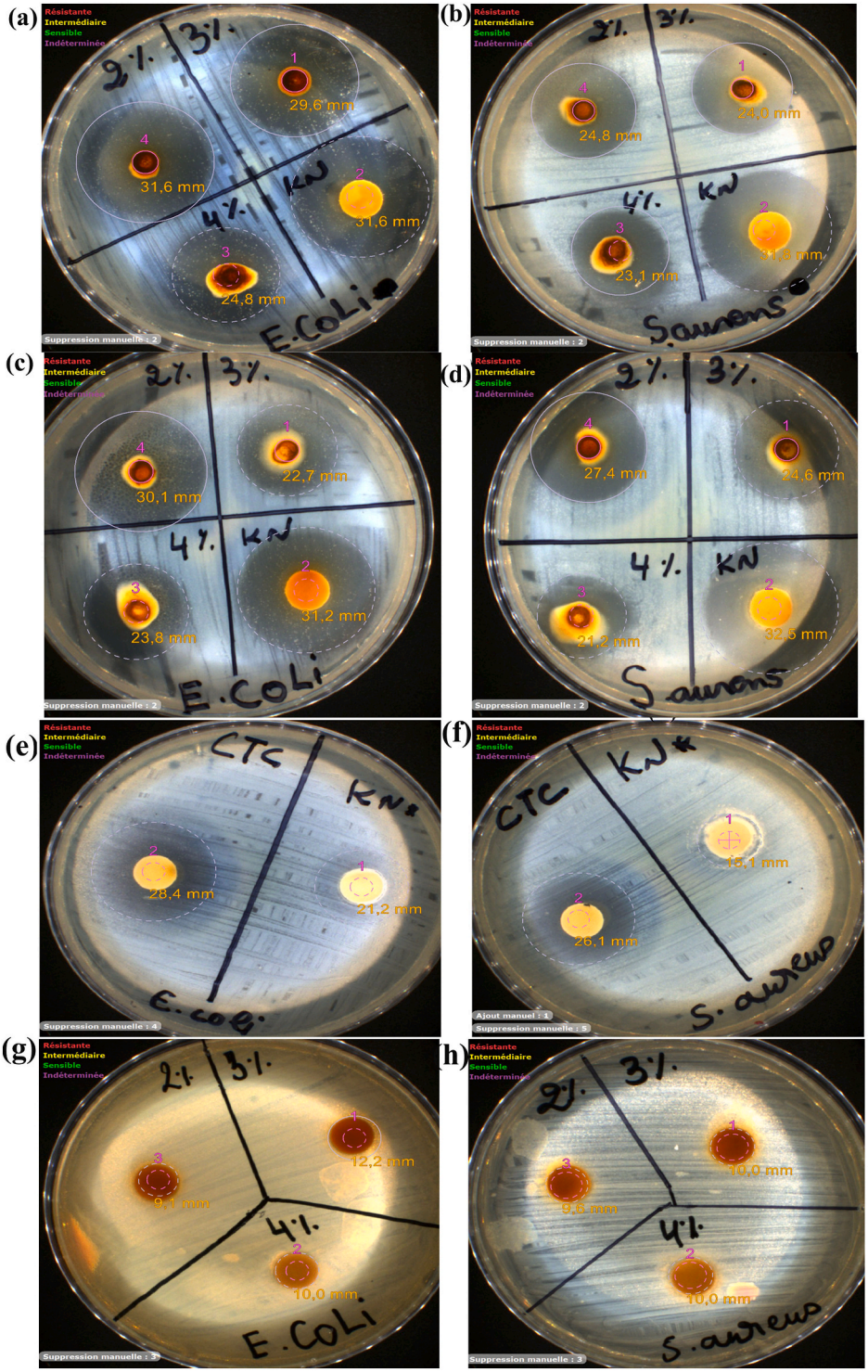


**Fig. 14.** Photographic images showing inhibition zones of Fe/Ca-Alg@K@CTC beads against *E. coli* (a) and *S. aureus* (b), and corresponding inhibition zones 4 h after CTC release against *E. coli*, (c) and *S. aureus* (d). Photographic images of inhibition zones of K and CTC against *E. coli* (e) and *S. aureus* (f), and Fe/Ca-Alg@K, Fe/Ca-Alg@K3, Fe/Ca-Alg@K4 beads against *E. coli* (g) and *S. aureus* (h).

demonstrated lower antibacterial activity against *S. aureus* compared to *E. coli*, they were still effective against *S. aureus*. It was also noteworthy that K@CTC exhibited robust antibacterial activity against both *E. coli* and *S. aureus*.

Both K and K-based alginate beads have demonstrated effectiveness in combating *E. coli* and *S. aureus*, and their antibacterial activities are greater than that of the pure CTC antibiotic drug (Fig. 14e–f). This may be attributed to the inherent antibacterial properties of the bead material itself. K without CTC loading exhibited intrinsic antibacterial activity, with inhibition zones of 21.2 mm and 15.1 mm in diameter against *E. coli* and *S. aureus*, respectively (Fig. 14e–f). K-based alginate beads (Fe/Ca-Alg@K3) also demonstrated antibacterial activity, with inhibition zones of 12.2 mm and 10 mm in diameter against *E. coli* and *S. aureus*, respectively (Fig. 14g–h). In summary, the superior antibacterial performance of beads stems not only from the inherent antibacterial activity of K itself but also relies on the effective modulation of drug release behavior by the SA concentration. These two aspects act synergistically to enhance the sustainability and stability of the antimicrobial effects. The findings of this study indicate that such composite materials hold potential for applications in medical dressings, controlled drug release systems, and related fields.

K-based alginate beads show promising potential as antibacterial agents, particularly against Gram-negative bacteria such as *E. coli*. However, their effectiveness against Gram-positive bacteria such as *S. aureus* is not very apparent and required higher concentrations to achieve similar effects. These observations emphasize the importance of further research to optimize the formulation and concentration for expanding the effectiveness spectrum of K-based alginate beads, particularly against Gram-positive bacteria.

## 4. Conclusion

Dual cation cross-linked alginate-kaolin hydrogel beads were successfully developed as an effective platform for the loading and sustained-release of CTC. Comprehensive morphological, structural, and thermal characterizations confirmed the stability and suitability of the composite system. Adsorption kinetics and isotherm analyses revealed that CTC loading onto beads involved physical and chemical mechanisms, including diffusion, cation-π bonds, n-π EDA bonding, hydrogen bonding, cation-n bridging, and electrostatic interactions. Kaolin incorporation and dual cation cross-linking strategy significantly enhanced drug encapsulation efficiency and loading capacity, while the alginate concentration modulated the cumulative release rate to achieve sustained release. At neutral pH, release kinetics followed a non-Fickian diffusion mechanism, governed by a combination of diffusion and polymer matrix relaxation. The beads exhibited potent antibacterial activity highlighting their potential for biomedical applications such as localized drug delivery and infection management. Overall, the integration of kaolin functionality with a dual cross-linking strategy provides a versatile approach to engineering advanced hydrogel-based drug delivery systems.

## CRediT authorship contribution statement

**Wei Liu:** Writing – review & editing, Writing – original draft, Methodology, Investigation, Data curation, Conceptualization. **Fizir Meriem:** Writing – review & editing, Writing – original draft, Software, Methodology, Investigation, Data curation, Conceptualization. **Touil Sami:** Project administration, Formal analysis. **Richa Amina:** Project administration, Funding acquisition. **Benaissa Fatiha:** Writing – review & editing, Methodology. **Bensettou Chaimaa:** Writing – review & editing, Methodology. **Douba Houda:** Writing – review & editing. **Tingzi Cao:** Methodology. **Aouameur Djamila:** Writing – review & editing, Conceptualization. **Xiaowei Tu:** Investigation. **Jing Ding:** Visualization, Funding acquisition. **Dramou Pierre:** Writing – review & editing, Writing – original draft, Visualization.

## Declaration of competing interest

All authors declare that they have no competing interests.

## Acknowledgements

This study received funding from a Scientific Research Fund of Zhejiang Provincial Education Department (Y202456477) and PRIMA2/CICLICA, a program backed by the European Union (Project ID 1727).

## Appendix A. Supplementary data

Supplementary data to this article can be found online at https://doi.org/10.1016/j.ijbiomac.2025.147827.

## Data availability

Data will be made available on request.

## References

[1] K. Kharga, S. Jha, T. Vishwakarma, L. Kumar, Current developments and prospects of the antibiotic delivery systems, Crit. Rev. Microbiol. 51 (1) (2025) 44–83.
[2] Y. Zhao, B. Liu, S.-y. Zhang, Y.-f. Wang, S.-r. Hasi, Y.-h. Qian, Z.-g. Gong, J.-m. Zhao, X.-l. Yang, Y.-t. Bai, Egg yolk-derived low-density lipoprotein: a potential drug delivery system to eradicate intracellular bacteria, Int. J. Biol. Macromol. 306 (2025) 141291.
[3] Z. Saadatidizaji, N. Sohrabi, R. Mohammadi, M.S. Amini-Fazl, Tetracycline hydrochloride loaded-alginate based nanoparticle-hydrogel beads for potential wound healing applications: in vitro drug delivery, release kinetics, and antibacterial activity, Int. J. Biol. Macromol. 264 (2024) 130653.
[4] O.S. Reddy, M. Subha, T. Jithendra, C. Madhavi, K.C. Rao, Curcumin encapsulated dual cross linked sodium alginate/montmorillonite polymeric composite beads for controlled drug delivery, Journal of Pharmaceutical Analysis 11 (2) (2021) 191–199.
[5] S. Boi, N. Rouatbi, E. Dellacasa, D. Di Lisa, P. Bianchini, O. Monticelli, L. Pastorino, Alginate microbeads with internal microvoids for the sustained release of drugs, Int. J. Biol. Macromol. 156 (2020) 454–461.
[6] Z. Touzout, N. Abdellaoui, A.S. Hadj-Hamou, Conception of pH-sensitive calcium alginate/poly vinyl alcohol hydrogel beads for controlled oral curcumin delivery systems. Antibacterial and antioxidant properties, Int. J. Biol. Macromol. 263 (2024) 130389.
[7] K. Nahar, M.K. Hossain, T.A. Khan, Alginate and its versatile application in drug delivery, J. Pharm. Sci. Res. 9 (5) (2017) 606.
[8] G.T. Grant, E.R. Morris, D.A. Rees, P.J. Smith, D. Thom, Biological interactions between polysaccharides and divalent cations: the egg-box model, FEBS Lett. 32 (1) (1973) 195–198.
[9] K.R. Reddy, M. Nagabhushanam, Process and parameters affecting drug release performance of prepared cross-linked alginate hydrogel beads for ezetimibe, Int J Pharm Pharm Sci 9 (2017) 254–262.
[10] F. Martínez-Gómez, J. Guerrero, B. Matsuhiro, J. Pavez, In vitro release of metformin hydrochloride from sodium alginate/polyvinyl alcohol hydrogels, Carbohydr. Polym. 155 (2017) 182–191.
[11] E. Rostami, Recent achievements in sodium alginate-based nanoparticles for targeted drug delivery, Polym. Bull. 79 (9) (2022) 6885–6904.
[12] A.F. Ahamed, M. Manimohan, N. Kalaivasan, Fabrication of biologically active fish bone derived hydroxyapatite and montmorillonite blended sodium alginate composite for in-vitro drug delivery studies, J. Inorg. Organomet. Polym. Mater. 32 (10) (2022) 3902–3922.
[13] J. Wang, C. Liu, Y. Shuai, X. Cui, L. Nie, Controlled release of anticancer drug using graphene oxide as a drug-binding effector in konjac glucomannan/sodium alginate hydrogels, Colloids Surf. B Biointerfaces 113 (2014) 223–229.
[14] L. Sukhodub, L. Sukhodub, M. Kumeda, Y.I. Prylutskyy, M. Pogorielov, M. Evstigneev, V. Kostjukov, N. Strutynska, L. Vovchenko, S. Khrapatiy, Single-walled carbon nanotubes loaded hydroxyapatite–alginate beads with enhanced mechanical properties and sustained drug release ability, Prog. Biomater. 9 (1) (2020) 1–14.
[15] M.I. Carretero, M. Pozo, Clay and non-clay minerals in the pharmaceutical industry: Part I. Excipients and medical applications, Applied Clay Science 46 (1) (2009) 73–80.
[16] H. Zhang, Y. Shi, X. Xu, M. Zhang, L. Ma, Structure regulation of bentonite-alginate nanocomposites for controlled release of imidacloprid, ACS omega 5 (17) (2020) 10068–10076.
[17] J. Čejka, W. Roth, M. Opanasenko, Two-dimensional Silica-based Inorganic Networks, 2017.
[18] S. Khazaei, B. Tanhaei, S.M. Khoshkho, M.N. Shahrak, Development of multifunctional agar/κ-carrageenan/kaolinite hydrogels: Role of tetracycline and marshmallow extract loading in antibacterial and controlled release properties, Int. J. Biol. Macromol. 308 (2025) 142092.

[19] M. Fizir, S. Touil, A. Richa, L. Wei, S. Douadia, R. Taibi, S. Cherifi, D. S. Mansuroglu, P. Dramou, Kaolin-iron cross-linked alginate beads for efficient phosphate removal from water: an initiation towards sustainable treatment of domestic and hydroponic wastewaters, Appl. Clay Sci. 256 (2024) 107430.
[20] Y. Wang, Z. Shen, H. Wang, Z. Song, D. Yu, G. Li, X. Liu, W. Liu, Progress in research on metal ion crosslinking alginate-based gels, Gels 11 (1) (2024) 16.
[21] J. de Freitas, A.P.G. Ferreira, É.T.G. Cavalheiro, Thermal analysis of tetracyclines: a review, J. Therm. Anal. Calorim. 149 (20) (2024) 11375–11387.
[22] G.R. Bardajee, A. Pourjavadi, S. Ghavami, R. Soleyman, F. Jafarpour, UV-prepared salep-based nanoporous hydrogel for controlled release of tetracycline hydrochloride in colon, J. Photochem. Photobiol. B Biol. 102 (3) (2011) 232–240.
[23] Z. Hadi, A.H. Navarchian, M. Rafienia, Synthesis of pH-responsive carboxymethyl chitosan for encapsulating tetracycline-HCl: morphology, drug release behavior and antibacterial activity of microcapsules, Journal of Drug Delivery Science and Technology 84 (2023) 104462.
[24] I.A. Kumar, N. Viswanathan, Fabrication of zirconium (IV) cross-linked alginate/kaolin hybrid beads for nitrate and phosphate retention, Arab. J. Chem. 13 (2) (2020) 4111–4125.
[25] A.H. Khalbas, T.M. Albayati, N.S. Ali, I.K. Salih, Drug loading methods and kinetic release models using of mesoporous silica nanoparticles as a drug delivery system: a review, South African Journal of Chemical Engineering 50 (1) (2024) 261–280.
[26] M. Gan, W. Zhang, S. Wei, H. Dang, The influence of mPEG-PCL and mPEG-PLGA on encapsulation efficiency and drug-loading of SN-38 NPs, Artificial cells, nanomedicine, and biotechnology 45 (2) (2017) 389–397.
[27] M. Fizir, P. Dramou, K. Zhang, C. Sun, C. Pham-Huy, H. He, Polymer grafted-magnetic halloysite nanotube for controlled and sustained release of cationic drug, J. Colloid Interface Sci. 505 (2017) 476–488.
[28] B. Kumar, P. Kumar, Synthesis and characterization of pH-sensitive nanocarrier based chitosan-g-poly (itaconic acid) for ciprofloxacin delivery for anti-bacterial application, Int. J. Biol. Macromol. 268 (2024) 131604.
[29] S. Sanaei-Rad, M.A. Ghasemzadeh, S.S. Aghaei, Synthesis and structure elucidation of ZnFe2O4/IRMOF-3/GO for the drug delivery of tetracycline and evaluation of their antibacterial activities, J. Organomet. Chem. 960 (2022) 122221.
[30] D. Rassis, I. Saguy, A. Nussinovitch, Collapse, shrinkage and structural changes in dried alginate gels containing fillers, Food Hydrocolloids 16 (2) (2002) 139–151.
[31] D.M. Roquero, A. Othman, A. Melman, E. Katz, Iron (III)-cross-linked alginate hydrogels: a critical review, Materials Advances 3 (4) (2022) 1849–1873.
[32] O. Churio, F. Pizarro, C. Valenzuela, Preparation and characterization of iron-alginate beads with some types of iron used in supplementation and fortification strategies, Food Hydrocoll. 74 (2018) 1–10.
[33] S. Banerjee, P.B. Tiwade, K. Sambhav, C. Banerjee, S.K. Bhaumik, Effect of alginate concentration in wastewater nutrient removal using alginate-immobilized microalgae beads: uptake kinetics and adsorption studies, Biochem. Eng. J. 149 (2019) 107241.
[34] M. Abd El-Ghaffar, M. Hashem, M. El-Awady, A. Rabie, Ph-sensitive sodium alginate hydrogels for riboflavin controlled release, Carbohydr. Polym. 89 (2) (2012) 667–675.
[35] A. Basu, S.S. Behera, S. Dash, S. Banerjee, S. Sarkar, C.K. Mohanty, N.K. Dhal, P. K. Parhi, S.K. Tripathy, A study on removal of Cr (III) from aqueous solution using biomass of Cymbopogon flexuosus immobilized in sodium alginate beads and its use as hydrogenation catalyst, J. Taiwan Inst. Chem. Eng. 102 (2019) 118–132.
[36] S. Sarkar, N. Tiwari, A. Basu, M. Behera, B. Das, S. Chakrabortty, K. Sanjay, M. Suar, T.K. Adhya, S. Banerjee, Sorptive removal of malachite green from aqueous solution by magnetite/coir pith supported sodium alginate beads: kinetics, isotherms, thermodynamics and parametric optimization, Environ. Technol. Innov. 24 (2021) 101818.
[37] N. Li, J. Gu, Z. Liu, H. Yu, Y. Wang, Z. Liu, Y. Li, New insight into multi-functional MOG@ COP/SA beads for co-adsorption and mono-detection in CTC-Cr (VI) co-contamination system and efficient anti-counterfeiting, Chem. Eng. J. 496 (2024) 154243.
[38] M. Liu, Y. Gao, Y. Wang, Y. Li, D. Zou, Status and opportunities in the treatment of tetracyclines from aquatic environments by metal-organic frameworks (MOFs) and MOFs-based composites, Materials Today Chemistry 26 (2022) 101209.
[39] A.M. Omer, E.M. Abd El-Monaem, G.M. El-Subruiti, M.M. Abd El-Latif, A. S. Eltaweil, Fabrication of easy separable and reusable MIL-125 (Ti)/MIL-53 (Fe) binary MOF/CNT/Alginate composite microbeads for tetracycline removal from water bodies, Sci. Rep. 11 (1) (2021) 23818.
[40] Y. Wang, Y. Gao, J. Gu, Z. Liu, N. Li, Z. Liu, Y. Li, Comprehensive insight into adsorption of chlortetracycline hydrochloride by room-temperature synthesized water-stable Zr-based metal-organic gel/sodium alginate beads, Environ. Res. 232 (2023) 116339.
[41] M.S. Salman, M.C. Sheikh, M.M. Hasan, M.N. Hasan, K.T. Kubra, A.I. Rehan, M. E. Awual, A.I. Rasee, R. Waliullah, M.S. Hossain, Chitosan-coated cotton fiber composite for efficient toxic dye encapsulation from aqueous media, Appl. Surf. Sci. 622 (2023) 157008.
[42] S. Erdem, M. Öztekin, Y.S. Açıkel, Investigation of tetracycline removal from aqueous solutions using halloysite/chitosan nanocomposites and halloysite nanotubes/alginate hydrogel beads, Environ. Nanotechnol. Monit. Manag. 16 (2021) 100576.
[43] W.J. Weber Jr., J.C. Morris, Kinetics of adsorption on carbon from solution, J. Sanit. Eng. Div. 89 (2) (1963) 31–59.
[44] Z. Falahian, F. Torki, H. Faghihian, Synthesis and application of polypyrrole/Fe3O4 nanosize magnetic adsorbent for efficient separation of Hg2+ from aqueous solution, Global Chall. 2 (1) (2018) 1700078.
[45] X. Liu, H. He, L. Wang, Synthesis of thermo-responsive Fe3O4/CMS-imprinted composite membranes for selective adsorption and controlled TC release, Sep. Purif. Technol. 367 (2025) 132779.
[46] G. Wang, X. Yue, S. Zhang, Q. Geng, J. Zheng, X. Xu, T. Li, Y. Pu, Y. Li, Y. Jia, La (III) loaded Fe (III) cross–linked chitosan composites for efficient removal of phosphate from wastewater: Performance and mechanisms, J. Clean. Prod. 379 (2022) 134833.
[47] M. Fizir, A. Richa, S. Touil, Y. Benmokadem, K. Boubekeur, B. Hallal, H. Drici, L. Wei, Preparation and application of a surfactant-modified Halloysite nanotubes for the adsorption of nitrates from aqueous solutions: kinetic and equilibrium studies, Environ. Prog. Sustain. Energy 42 (2) (2023) e13995.
[48] S. Hu, X. Lin, Y. Zhang, R. Huang, Y. Qu, X. Luo, J. Zhou, Preparation and application of alginate-Ca/attapulgite clay core/shell particle for the removal of uranium from aqueous solution, J. Radioanal. Nucl. Chem. 314 (2017) 307–319.
[49] A. Balakrishnan, M. Chinthala, R.K. Polagani, 3D kaolinite/g-C3N4-alginate beads as an affordable and sustainable photocatalyst for wastewater remediation, Carbohydr. Polym. 323 (2024) 121420.
[50] O.-H. Kwon, J.-O. Kim, D.-W. Cho, R. Kumar, S.H. Baek, M.B. Kurade, B.-H. Jeon, Adsorption of As (III), As (V) and Cu (II) on zirconium oxide immobilized alginate beads in aqueous phase, Chemosphere 160 (2016) 126–133.
[51] A. Guesmi, N.B. Hamadi, W. Abd El-Fattah, A. Subaihi, A.A. Alluhaybi, M.G. El-Desouky, A.A. El-Bindary, Efficient removal of ciprofloxacin in aqueous solutions by magnetic se-MOF embedded within a biopolymer (chitosan/alginate): adsorptive behavior, mechanism study, and optimization using box-behnken design, Int. J. Biol. Macromol. 314 (2025) 144274.
[52] P. Tordi, F. Ridi, P. Samorì, M. Bonini, Cation-alginate complexes and their hydrogels: a powerful toolkit for the development of next-generation sustainable functional materials, Adv. Funct. Mater. 35 (9) (2025) 2416390.
[53] M.F. Abed, A.A. Faisal, Calcium/iron-layered double hydroxides-sodium alginate for removal of tetracycline antibiotic from aqueous solution, Alex. Eng. J. 63 (2023) 127–142.
[54] T. Shahwan, H.N. Erten, Characterization of Sr2+ uptake on natural minerals of kaolinite and magnesite using XRPD, SEM/EDS, XPS, and DRIFT, Radiochim. Acta 93 (4) (2005) 225–232.
[55] Q. Zhang, Z. Yan, J. Ouyang, Y. Zhang, H. Yang, D. Chen, Chemically modified kaolinite nanolayers for the removal of organic pollutants, Appl. Clay Sci. 157 (2018) 283–290.
[56] X. Zhang, X. Lin, Y. He, Y. Chen, X. Luo, R. Shang, Study on adsorption of tetracycline by Cu-immobilized alginate adsorbent from water environment, Int. J. Biol. Macromol. 124 (2019) 418–428.
[57] P.-H. Chang, R. Mukhopadhyay, B. Sarkar, Y.-C. Mei, C.-H. Hsu, Y.-M. Tzou, Insight and mechanisms of tetracycline adsorption on sodium alginate/montmorillonite composite beads, Appl. Clay Sci. 245 (2023) 107127.
[58] Q. Li, P. Fan, Z. Hao, S. Ni, Q. Wu, L. Li, Fluorimetric determination of tetracycline antibiotics in animal derived foods using boron and nitrogen co-doped ceria-based nanoparticles, Microchim. Acta 191 (3) (2024) 147.
[59] Y. Zhao, Z. Cao, J. Li, B. Bai, Y. Jia, Q. Wang, H. Cheng, Selective adsorption and photocatalytic degradation of chlortetracycline hydrochloride using a La2Ti2O7/acid-modified coal-bearing strata kaolinite composite, Appl. Surf. Sci. 609 (2023) 155489.
[60] M.M. Ivanović, L.M. Kljajević, M. Nenadović, N. Bundaleski, I. Vukanac, B.Ž. Todorović, S.S. Nenadović, Physicochemical and radiological characterization of kaolin and its polymerization products, Mater. Constr. 68 (330) (2018).
[61] M.-f. Li, Y.-g. Liu, S.-b. Liu, G.-m. Zeng, X.-j. Hu, X.-f. Tan, L.-h. Jiang, N. Liu, J. Wen, X.-h. Liu, Performance of magnetic graphene oxide/diethylenetriaminepentaacetic acid nanocomposite for the tetracycline and ciprofloxacin adsorption in single and binary systems, J. Colloid Interface Sci. 521 (2018) 150–159.
[62] X. Liu, X. Zhao, H. He, J. Zhang, Y. Zhang, L. Wang, Comprehensive study on amino-modified salix wood powder membranes: preparation, adsorption mechanism and desorption conditions for efficient chlortetracycline removal, ChemNanoMat 11 (1) (2025) e202400515.
[63] S.A. Akinyemi, B.B. Nyakuma, O.F. Adebayo, A.T. Kayode, A. Jauro, O. A. OlaOlorun, A.O. Aturamu, H.Y. Madukwe, A.K. Adegoke, T.A.T. Abdullah, Geochemistry, mineralogy and thermal analyses of Cretaceous coals from the Benue Trough basin Nigeria: Reconnaissance assessments, J. Afr. Earth Sci. 178 (2021) 104167.
[64] Y. Hu, C. Pan, X. Zheng, S. Liu, F. Hu, L. Xu, G. Xu, X. Peng, Removal of ciprofloxacin with aluminum-pillared kaolin sodium alginate beads (CA-Al-KABs): Kinetics, isotherms, and BBD model, Water 12 (3) (2020) 905.
[65] T. Bai, K. Zhao, Q. Gao, M. Qi, Y. Zhang, Z. Lu, H. Zhao, H. Gao, J. Wei, Kaolin/CaAlg hydrogel thin membrane with controlled thickness, high mechanical strength, and good repetitive adsorption performance for dyes, Ind. Eng. Chem. Res. 59 (11) (2020) 4958–4967.
[66] N. Marzban, A. Moheb, S. Filonenko, S.H. Hosseini, M.J. Nouri, J.A. Libra, G. Farru, Intelligent modeling and experimental study on methylene blue adsorption by sodium alginate-kaolin beads, Int. J. Biol. Macromol. 186 (2021) 79–91.
[67] D.P. Kgabi, A.A. Ambushe, Characterization of South African bentonite and kaolin clays, Sustainability 15 (17) (2023) 12679.
[68] Q. Sun, B. Aguila, J. Perman, A.S. Ivanov, V.S. Bryantsev, L.D. Earl, C.W. Abney, L. Wojtas, S. Ma, Bio-inspired nano-traps for uranium extraction from seawater and recovery from nuclear waste, Nat. Commun. 9 (1) (2018) 1644.
[69] S.S. Priya, K. Radha, A review on the adsorption studies of tetracycline onto various types of adsorbents, Chem. Eng. Commun. 204 (8) (2017) 821–839.

[70] Y. Chen, S. Hu, C. Shen, L. Zhang, C. Yi, Y. Chen, G.-S. Liu, L. Chen, Z. Chen, Y. Luo, Hyperbolic-metamaterial-based optical fiber SPR sensor enhanced by a smart hydrogel for perspiration pH measurements, Nano Lett. 25 (1) (2024) 129–137.
[71] Z. Sayyar, G.R. Mahdavinia, A. Khataee, Dual-drug (Curcumin/Ciprofloxacin) loading and release from chitosan-based hydrogels embedded with magnetic Montmorillonite/Hyaluronic acid for enhancing wound healing, J. Biol. Eng. 17 (1) (2023) 66.
[72] Q. Wang, X. Xie, X. Zhang, J. Zhang, A. Wang, Preparation and swelling properties of pH-sensitive composite hydrogel beads based on chitosan-g-poly (acrylic acid)/vermiculite and sodium alginate for diclofenac controlled release, Int. J. Biol. Macromol. 46 (3) (2010) 356–362.
[73] R. Han, H. He, Y. Lu, H. Lu, S. Shen, W. Wu, Oral targeted drug delivery to post-gastrointestinal sites, J. Control. Release 370 (2024) 256–276.
[74] G.O. Akalin, Alginate/carboxymethylcellulose-based hydrogels as pH-sensitive drug delivery systems: facile production with enhanced degradation, thermal and mechanical properties, Iran. Polym. J. 32 (8) (2023) 1013–1032.
[75] L. Tian, M.R. Abukhadra, A.S. Mohamed, A. Nadeem, S.F. Ahmad, K.E. Ibrahim, Insight into the loading and release properties of an exfoliated kaolinite/cellulose fiber (EXK/CF) composite as a carrier for oxaliplatin drug: cytotoxicity and release kinetics, ACS Omega 5 (30) (2020) 19165–19173.
[76] Z. Mao, J. Chen, Y. Wang, J. Xia, Y. Zhang, W. Zhang, H. Zhu, X. Hu, H. Chen, Copper metal organic framework as natural oxidase mimic for effective killing of Gram-negative and Gram-positive bacteria, Nanoscale 14 (26) (2022) 9474–9484.